Structural control, magmatic-hydrothermal evolution and formation of hornfels-hosted, intrusion-related gold deposits: Insight from the Thaghassa deposit in Eastern Anti-Atlas, Morocco.

Johann Tuduri, Alain Chauvet, Luc Barbanson, Mohamed Labriki, Michel Dubois, Pierre-Henri Trapy, Abdeltif Lahfid, Marc Poujol, Jérémie Melleton, Lakhlifi Badra, et al.

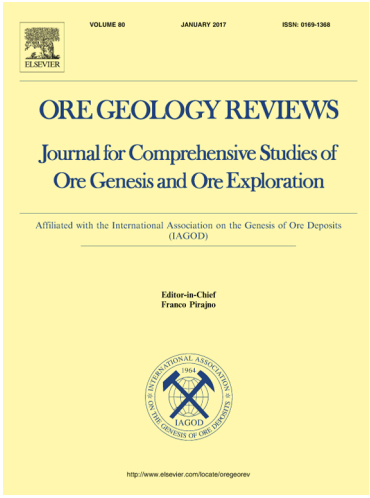

Structural control, magmatic-hydrothermal evolution and formation of hornfels-hosted, intrusion-related gold deposits: Insight from the Thaghassa deposit in Eastern Anti-Atlas, Morocco.

Johann Tuduri, Alain Chauvet, Luc Barbanson, Mohamed Labriki, Michel Dubois, Pierre-Henri Trapy, Abdeltif Lahfid, Marc Poujol, Jérémie Melleton, Lakhlifi Badra, Aomar Ennaciri, Lhou Maacha

PII: S0169-1368(17)30407-9
DOI: https://doi.org/10.1016/j.oregeorev.2018.04.023
Reference: OREGEO 2567

To appear in: *Ore Geology Reviews*

Received Date: 18 May 2017
Revised Date: 18 April 2018
Accepted Date: 23 April 2018

Please cite this article as: J. Tuduri, A. Chauvet, L. Barbanson, M. Labriki, M. Dubois, P-H. Trapy, A. Lahfid, M. Poujol, J. Melleton, L. Badra, A. Ennaciri, L. Maacha, Structural control, magmatic-hydrothermal evolution and formation of hornfels-hosted, intrusion-related gold deposits: Insight from the Thaghassa deposit in Eastern Anti-Atlas, Morocco., *Ore Geology Reviews* (2018), doi: https://doi.org/10.1016/j.oregeorev.2018.04.023

Structural control, magmatic-hydrothermal evolution and formation of hornfels-hosted, intrusion-related gold deposits: Insight from the Thaghassa deposit in Eastern Anti-Atlas, Morocco.

JOHANN TUDURI[A,*], ALAIN CHAUVET[B], LUC BARBANSON[C], MOHAMED LABRIKI[D], MICHEL DUBOIS[E], PIERRE-HENRI TRAPY[F], ABDELTIF LAHFID[A], MARC POUJOL[G], JÉRÉMIE MELLETON[A], LAKHLIFI BADRA[H], AOMAR ENNACIRI[D], LHOU MAACHA[D],

[A] *BRGM, 3 avenue Claude Guillemin, BP36009, 45060 Orléans Cedex2, France*

[B] *Géosciences Montpellier, cc. 060, Université de Montpellier 2, 34095 Montpellier Cedex 5, France*

[C] *Université d'Orléans, Institut des Sciences de la Terre d'Orléans, UMR 7327, 45071 Orléans, France*

[D] *MANAGEM, Twin Center, BP 5199, 20100, Casablanca, Maroc*

[E] *Laboratoire Génie Civil et Géo-Environnement (LGCgE / EA 4515), Université Lille 1, building SN5, 59655 Villeneuve d'Ascq, France*

[F] *Department of Civil, Geological & Mining Engineering, Polytechnique Montréal, Montréal QC H3C 3A7, Canada*

[G] *Géosciences Rennes, UMR CNRS 6118, Université de Rennes 1, OSUR, Campus de Beaulieu, 35042 Rennes Cedex, France*

[H] *Université Moulay Ismaïl, Faculté des sciences, BP 11201 Zitoune, 50 000 Meknes, Maroc*

*j.tuduri@brgm.fr

Abstract

In the Moroccan Eastern Anti-Atlas, the Thaghassa intrusion-related gold deposit is hosted in hornfelsed metasedimentary rocks that lie adjacent to the Ikniwn granodiorite. Fields studies reveal three tectono-magmatic stages controlling the formation of the deposit. **i**) The first stage refers to the top-to-the-south asymmetry and the syn-kinematic Ikniwn pluton emplacement controlled by a compressional or transpressional strain regime. **ii**) The second stage is characterized, from older to younger and further away from the intrusion, by: metatexite with leucocratic stromatic bands, aplo-pegmatite sills, intermediate veinlets composed of quartz, K-feldspar and muscovite, and then gold-bearing striped foliation-veins. All these features are assumed to have been emplaced during a large-scale ENE-WSW dextral shearing process that results from an ESE-WNW shortening direction during transtensive tectonics. We suggest that the progressive and continuous shearing was initiated since the aplo-pegmatite stage and achieved during the hydrothermal phase. The existence of intermediate veins characterized by quartz-rich core and apatite-muscovite-feldspar-rich rims demonstrates the progressive evolution from the magmatic to the hydrothermal stage and evidence for the persistence of the magmatic character, at least until the onset of the hydrothermal process. **iii**) The late stage developed large volcanic dyke swarm and brittle faulting.

Zircon U-Pb LA-ICP-MS dating yields a Concordia age of 563.5 ± 6.3 Ma for the Ikniwn granodiorite intrusion. The fluid inclusions data besides the mineral thermometry indicate that two main types of fluids can been highlighted: **i**) a hot aquo-carbonic (H_2O-NaCl-CO_2) fluid with N_2 and CH_4, evolving from vapour-rich N_2 and CH_4 inclusions for the magmatic stage (~550°C) to CH_4-CO_2 biphased inclusions for the ongoing hydrothermal stage (~450-300°C) and **ii**) an always secondary low T (~200°C) saline aqueous type (probably NaCl) free from volatiles, with very variable salinity. Eventually, we highlight that in the hornfels-hosted IRG deposits, fluid sources may originate from both magmatic processes and devolatization of the metamorphic host rocks.

Keywords

IRGD; migmatite; hornfels; magmatic-hydrothermal transition; Anti-Atlas; Morocco

1. Introduction

Within orogenic domains, fluid circulation associated with magmatism is frequently invoked as being responsible for the development of large hydrothermal and mineralized veins systems (*e.g.*, Bierlein and McKnight, 2005; Eldursi et al., 2009; Jensen and Barton, 2000; Lang and Baker, 2001; Thompson and Newberry, 2000). Thus, while granites are supposed to provide the heat and eventually the fluids involved in the leaching processes of the surrounding rocks, tectonism may create structures that can act as preferential drains for fluid flow and (or) as traps for the mineralization. In the literature (*e.g.*, Baker and Lang, 2001; Hart, 2007; Lang and Baker, 2001; Thompson et al., 1999), intrusion-related gold deposits (IRGD) are characterized by their: **i**) location within deformed accretionary to collisional, subduction-related terranes; **ii**) close spatial and temporal association with small stocks (including swarms of dykes and/or sills) or large plutons of calc-alkaline composition and of relatively low to intermediate oxidation state, which are transitional between the ilmenite and magnetite series; and **iii**) arrays of auriferous sheeted quartz veins with a low sulfide content. Fluids invoked at the origin of the Au (±As, Sb, Bi, Cu, Zn, Sn, W, Mo, Te) mineralization are water with a significant CO_2 content and salinities up to saturation. In addition to CO_2, CH_4, N_2 and H_2S components may be abundant. There are common patterns showing early carbonic fluids evolving toward late aqueous brines (*e.g.*, Baker and Lang, 2001 and references herein). Regarding the source for the fluids, the debate is still open concerning the role of the magmatic fluids in the formation of hydrothermal and mineralized systems. Arguments against a magmatic origin for the fluids and metals are mainly based on fluid inclusion studies and isotopic data on quartz-bearing veins. They highlight the meteoric and/or metamorphic signatures of the fluids and suggest a complete decoupling between magmatism and hydrothermalism (*e.g.*, Boiron et al., 2003; Cepedal et al., 2013; Essarraj et al., 2001; Vallance et al., 2003). In such cases, heat production from the granitoids is supposed to only generate thermal convection cells and thus the fluids scavenge gold and other metals from the metamorphic or sedimentary host rocks (Boiron et al., 2003; Rowins et al., 1997).

Arguments in favour of a magmatic origin for the fluids are the systematic spatial association between granite and hydrothermal systems, gold content of silicic melt inclusions, and fluid compositions dominated by a magmatic component (Baker and Lang, 2001; Hart et al., 2004; Lang and Baker, 2001; Mair et al., 2006, 2011; Marcoux et al., 2015; Mustard, 2001; Mustard et al., 2006; Tunks and Cooke, 2007). The magmatic-hydrothermal connection remains insufficiently demonstrated in the literature. Most of the works applied to this thematic are mainly focused around analytical and experimental studies on fluid and melt inclusions of mineralized magmatic systems (*e.g.*, Halter and Webster, 2004, Mair et al., 2006; Mustard et al., 2006).

By contrast, the lack of significant studies devoted to the characterization of pluton-related structural controls and of mineralized veins systems encountered in the vicinity of the granitic intrusions has been already highlighted (Halter and Webster, 2004; Lang and Baker, 2001). Indeed, relatively few studies have been focused on geometrical, textural and mineralogical analysis of a global vein system with the aim to demonstrate the existence of a transitional stage between magmatic and hydrothermal events (*e.g.*,

Chauvet et al., 2012; Gloaguen et al., 2014; Kontak and Kyser, 2011; Thorne et al., 2008). The aim of this study is to present and discuss the formation of aplo-pegmatitic sills and quartz-bearing vein systems in the light of their geometry, mineralogy and internal texture. Taking into account structural, textural, mineralogical, preliminary microthermometric study and relative chronological constraints, a model in which a progressive and continuous tectonic event controlling magmatic to hydrothermal vein emplacement is proposed and discussed. The consequences concerning the eventual persistence of a magmatic character during the initiation of the hydrothermal vein systems, and thus the existence of a link between magmatism and hydrothermalism are discussed.

2. Regional geology framework

2.1. Outline of the geology of the Moroccan Anti-Atlas

The Anti-Atlas area in Morocco is the most important segment of the major Neoproterozoic, also known as Pan-African, belt system in the northern part of the West African Craton (Fig. 1a). Although it has been affected by the Variscan orogeny (Burkhard et al., 2006), this mountain range is currently at an altitude exceeding 1000 m in large areas due to Caenozoic uplift and related erosion (Gouiza et al., 2017; Missenard et al., 2006). As a consequence, the Anti-Atlas area present vast exposures of WSW-ENE trending inliers, also called "boutonnières", which consist of erosional Proterozoic basement that are unconformably overlain by Phanerozoic, mainly lower Palaeozoic, sequences (Fig. 1b). During Precambrian times, the Anti-Atlas mountains recorded two major orogenic stages: one during the Palaeoproterozoic (Eburnean cycle) from about 2.1 to 2.0 Ga that can only be seen in the western part of the Anti-Atlas mountains and the other one during the Neoproterozoic (Pan-African cycle) between 885 and 540 Ma *(e.g.*, Barbey et al., 2004; Choubert, 1963; Gasquet et al., 2005; Hefferan et al., 2014; Thomas et al., 2004). The Pan-African orogeny is described as a complex amalgamation of accreted oceanic and arc terranes and is characterized by three main tectono-magmatic events (Choubert, 1963; Hefferan et al., 2014; Leblanc and Lancelot, 1980; Saquaque et al., 1992; Walsh et al., 2012). **i)** The first one corresponds to oceanic basin closure, oceanic subduction and arc-craton accretion, coeval with calc-alkaline magmatism and ophiolite obduction. This event is supposed to have occurred between 770 and 630 Ma and is mainly observable in the Central Anti-Atlas (Blein et al., 2014; El Hadi et al., 2010; Inglis et al., 2005; Thomas et al., 2002; Walsh et al., 2012). **ii**) Secondly, the development of an active margin along the amalgamated West African Craton was responsible for an intense high-K calc-alkaline magmatism (gabbros, diorites, granodiorites, granites and related volcanic rocks) and transpressive tectonics between *ca.* 615 and 560 Ma (Gasquet et al., 2005; Hefferan et al., 2014; Inglis et al., 2004; Thomas et al., 2002; Tuduri, 2005; Walsh et al., 2012). **iii**) At last, emplacement of late to post-orogenic granites and cogenetic volcanic and volcaniclastic cover between *ca.* 560 and 540 Ma together with subsequent transtensional tectonics are also developed in the whole Anti-Atlas (Gasquet et al., 2005; Thomas et al., 2004; Tuduri, 2005; Walsh et al., 2012). A transition from transpressive to transtensive tectonics is also described at approximately 560 Ma (Walsh et al., 2012). There is still an ongoing debate

for the origin of this late magmatic event which is either described as arc-related (Walsh et al., 2012) or as post-orogenic related to an asthenospheric rise beneath the West African Craton, without any subduction context (Gasquet et al., 2005).

In the Eastern Anti-Atlas (Jbel Saghro) Palaeoproterozoic terranes are not exposed, the oldest rocks outcropping consisting in Cryogenian basins hosting turbiditic deposits (shales and greywackes) with interbedded mafic lavas mainly deposited at the onset of the Pan-African orogeny (Fekkak et al., 2001; Ouguir et al., 1996). Such rocks are exposed from East to West within the Imiter, Boumalne, Qal'at Mgouna and Sidi Flah areas (Fig. 2). They are slightly deformed and metamorphosed into the greenschist facies (Fekkak et al., 2001; Hindermeyer, 1953) and are unconformably overlain by a thick and widespread Ediacaran volcanic and volcaniclastic sequence (Fig. 2). Both Cryogenian and Ediacaran units are intruded by Pan-African plutons (Fig. 2). A three stages magmatic evolution model is proposed for the Jbel Saghro area. **i**) The first stage remains unclear only evidenced by poorly defined U-Pb zircon geochronology on calc-alkaline tonalite, diorite and granodiorite intrusions (*i.e.*, >615 Ma; Massironi et al., 2007; O'Connor et al., 2011; Schiavo et al., 2007). The last two stages are characterized by high-flux of high-K calc-alkaline magmatism (granodioritic and granitic plutons), as well as ignimbrite flare up (Tuduri, 2005). **ii**) The second stage (615-560 Ma) was dominated by dioritic to granitic plutons mainly emplaced between 590 and 560 Ma, as well as volcanic rocks (ignimbrites, lava flows, dyke swarms) mostly emplaced between 580 and 560 Ma (Cheilletz et al., 2002; De Wall et al., 2001; Tuduri, 2005; Walsh et al., 2012) in an ash-flow caldera environment (Tuduri, 2005; Walsh et al., 2012). **iii**) The third and final stage spanning from 560 to 540 Ma and outcropping in the central, southern and eastern Saghro, was characterized by more evolved and slightly alkaline pink granitic plutons, lava flows, ash-flow tuffs and rhyolite dykes with volcaniclastic and clastic sedimentary rocks (Cheilletz et al., 2002; Walsh et al., 2012).

2.2. *Geology of the Boumalne area*

The Thaghassa prospect, the location of our study, is situated in the central Jbel Saghro, 25 km southeast of the city of Boumalne (Figs. 2 and 3a). It belongs to the southern part of the Boumalne inlier basin (Boumalne inlier), an area dominated by Cryogenian turbidites with intercalated thin mafic lava layers (Fig. 3a, Fekkak et al., 2002). The overall style of the deformation suggests a north-plunging syncline with an ENE-WSW axial plane and a dip of 50-60° to the NNW (Benkirane, 1987). The regional metamorphism is low and belongs to the (sub)-greenschist facies (Fekkak et al., 2002; O'Connor et al., 2011), although Bienziane (2007) has reported the presence of amphibole and garnet in addition to chlorite and sericite. Several volcanic units also occur and consist of andesitic to rhyo-dacitic volcanic and volcaniclastic rocks including subsequent emplacement of ignimbrites. Two main units are observed. On the eastern part of the map in the Jbel n'Habab (Fig. 3a), porphyritic andesite with subordinate dacitic and rhyolitic tuffs have been identified and dated at 570±7 Ma (U-Pb on zircon; O'Connor et al., 2011). Silicic volcanic rocks outcrop in the western part of the map in the Tislit n'Ouzarzam hills. They mostly

consist of flow-banded rhyolite and welded rhyodacitic ash flow tuffs dated at 564±6 Ma (U-Pb on zircon; O'Connor et al., 2011).

Four plutons are exposed in this area, although only three intrude the Boumalne inlier Cryogenian metaturbiditic (BICM) rocks: they are from the largest to the smallest (Fig. 3a):

i) The large Ikniwn intrusion generally displays homogeneous, massive, and medium- to coarse-grained biotite-amphibole granodiorite. Contacts with the BICM rocks are generally intrusive. In some places, O'Connor et al. (2011) reported chilled margins towards the contact and the development of granitic and siliceous veins that may occur in both lithologies. The western margin of the pluton is overlain unconformably by the Tislit n'Ouzarzam volcaniclastic rocks. Samples exhibit plagioclase, amphibole, quartz, biotite, K-feldspar, and accessory apatite, zircon, magnetite and ilmenite. In the western part of the pluton, scarce elongated mafic enclaves and xenoliths of metasediments are roughly oriented N-S. Anisotropy of magnetic susceptibility studies, performed in order to characterize the internal fabrics of the pluton (Errami and Olivier, 2012), revealed a regular pattern of magmatic foliations (N045°E 65°NW) and lineations (N170°E 50°N) in the north western part of the pluton. Magnetic features of the whole Ikniwn intrusion suggest a syn-tectonic setting influenced by a regional transpressional event combining top-to-the-SE motions and E–W dextral shearing (Errami and Olivier, 2012). U-Pb zircon geochronology shows poorly defined ages ranging from 690±57 Ma (O'Connor et al., 2011) to 567±41 Ma (Mrini, 1993), as well as a poorly constrained Rb-Sr whole-rock isochron age of 534±73 Ma (Mrini, 1993).

ii) The large Isk n'Alla intrusion is a medium-grained, massive, granite with a pink-red colour. Exposure is mainly restricted to the southernmost section of the map (Fig. 3a). This pluton is in contact with both the Ikniwn granodiorite and the Tislit n'Ouzarzam volcaniclastic rocks. These contacts are largely faulted, although O'Connor et al. (2001) suggested that the Isk n'Alla granite intrudes both units because of the presence of a chilled margin and hornfels at the contact. This pink granite is characterized by quartz, K-feldspar, albite, biotite, amphibole, pyroxene, and accessory apatite and zircon, with scarce monazite, molybdenite and uranothorite. A zircon U-Pb study yielded a weighted average date of 555±4 Ma (De Wall et al., 2001) in the study area. Another comparable weighted average date of 559±5 Ma (Walsh et al., 2012) was found for the westernmost part of the intrusion. Both dates were interpreted as the age of the granite emplacement. This age is in agreement with a Rb-Sr whole-rock isochron age of 550 Ma (no error reported; Mrini, 1993).

iii) The Tiounouine pink microgranite (550 Ma, no error reported, whole rock Rb/Sr isochron; Mrini, 1993), is characterized by a medium-grained porphyritic texture and composed of K-feldspar phenocrysts, quartz and rare plagioclase, with minor apatite and zircon. It intrudes both the BICM rocks and the rhyolitic tuffs of the Tislit n'Ouzarzam area in the west.

iv) Finally, the small and highly altered Taourirt Tamellalt intrusion occurs only within the BICM rocks and is described as medium- to coarse-grained leucogranite (Massironi et al., 2007) characterized by the presence of two micas (biotite and muscovite), quartz, K-feldspar and albite. Accessory minerals are garnet, apatite, titanite, ilmenite and zircon (Benkirane, 1987). The emplacement age of this leucogranite

is herein debated (see discussion) because it is poorly constrained and the available ages range between 520 and 650 Ma (550±33 Ma, whole-rock Rb-Sr; Mrini, 1993 and 645±12 Ma, U-Pb zircon; Massironi et al., 2007).

Within the BICM rocks, contact metamorphic aureoles have developed around the different intrusions (Fig. 3a). They are often characterized by the presence of prominent porphyroblasts of probable retrogressed cordierite and (or) andalusite (Benkirane, 1987). Such aureoles are usually narrow, except along the Ikniwn intrusion where contact minerals define a 1.5 km-wide thermal aureole (Benkirane, 1987; O'Connor et al., 2011). Note that Hindermeyer (1953) suggested wider thermal areas up to 5-6 km around the diorite and granodiorite intrusions within the Jbel Saghro. The southernmost part of the Boumalne inlier shows a very intense ENE-WSW trending dyke swarm with various compositions and textures (flow banded dacite, andesite and dolerite-microgabbro) that intrudes both the BICM rocks, the eastern most part (*i.e.*, Jbel n'Habab volcaniclastic unit) and the Ikniwn granodiorite (Fig. 3a). Because the acid and basic dykes cross-cut each other, O'Connor et al. (2011) suggested a unique and short event for the emplacement of this swarm. Note that this dyke swarm does not cut the Isk n'Allah pink granite (Figs. 2 and 3a).

2.3. *Tungsten, gold, silver and base metal-bearing mineral occurrences*

The Jbel Saghro area hosts numerous precious and base metal deposits (Fig. 2). The most famous are the giant Ag Imiter mine (8.5 Mt @ 700 g/t Ag; Essaraj et al., 2016; Tuduri et al., 2006), the Cu Bouskour mine (21 Mt @ 1.3% Cu; Bouabdellah et al., 2016) and the Au(-Ag) Bou Isserfane mine (0.5 Mt @ 1.8 g/t Au; Tuduri, 2005) but also the now closed Cu-Ag Tizi Moudou (1.5 Mt at 2 % Cu, 250 g/t Ag; Al Ansari et al., 1997) and Cu-Au-Ag Tiwit (1.06 Mt at 8g/t Au, 65 g/t Ag, ~0.4% Cu; Al Ansari et al., 1997) mines. In the Boumalne inlier, the Taourirt-Tamellalt prospect was investigated for W (scheelite) and Au between 1975 and 1982 by BRPM (Moroccan geological survey), but with only limited success. In the prospect, a greisen alteration halo is strongly developed and controlled by N070°E-trending sheeted quartz veins that contains quartz, muscovite, scheelite, cassiterite, stannite, molybdenite, arsenopyrite, pyrite, sphalerite, galena and gold (Benkirane, 1987). Then, in the mid 1990's, BRPM and Reminex (a subsidiary of the Managem group) reinterpreted the regional geology. This led to the exploration of a large part of the Jbel Saghro area and to the discovery of several Au showings, such as the Thaghassa prospect of interest here, with drill core data showing the presence of 1 to 2 m at 5 g/t Au, and up to 400 g/t Ag (Managem group, unpublished data).

3. Analytical methods

3.1. *Mineral chemistry*

Mineral compositions were determined with Cameca SX50 and Camebax electron probe micro-analyser (EPMA) at the ISTO-BRGM laboratory in Orléans, equipped, respectively, with five and four wavelength dispersive spectrometers using both natural and synthetic standards: K (natural orthoclase), Mn and Ti (synthetic $MnTiO_3$), Na and Si (natural albite), Fe (synthetic Fe_2O_3), Al (synthetic corundum), V and Cl (natural vanadinite), Mg (natural

olivine), Cr (synthetic Cr2O3), Ca (natural andradite) and F (natural topaz). An accelerating voltage of 15 kV with a beam current of 12 nA and a beam diameter of about 1-2 µm, were used to analyse micas and others associated silicates. Counting times on peaks were twice that of background, with 10 s for each element, except for F and Cl for which counting times were 15 s. The sample database includes over 440 analyses of micas, garnet, feldspars, tourmaline, apatite, chlorite, prehnite and epidote. Sulfides and associated mineral compositions were done at 20kV with a beam current of 20nA, using the following X-ray lines and standards: Cu (metal), S and Fe (natural pyrite), Sb (natural stibnite), As (synthetic AsGa), Zn (natural sphalerite), Pb (natural galena), Mn (synthetic $MnTiO_3$), Cd (metal), Co (metal), Hg (natural cinnabar), Ag (metal), Ni (metal), Bi (metal), W (metal), Mo (metal), Se (metal), Au (metal), Te (metal) and In (natural roquesite). An accelerating voltage of 20 kV,with a beam current of 20 nA and a beam diameter of about 1-2 µm was used to analyse the minerals. Counting times on peaks were twice that of background, with 10 s for each element, except for Se, Ag, Au (Lα), Te and In for which a 30 s counting time was used. Analyses were undertaken in order to detect traces of gold (Au Mα) or silver within pyrite and arsenopyrite; they were completed with 80 s of counting time. The sample database includes over 450 analyses among which over 250 of the analyses are pyrite. For all the chemical compositions, only the significant values with an accuracy of 95% [(peak-background) × counting time > 2 × √ (background × counting time)] were retained.

In the case of the white micas, a total of 159 microprobe analyses were obtained from the Thaghassa area. Because electron microprobe data cannot provide the oxidation state of Fe nor the contents for all the light elements, and in order to compare the substitution mechanisms in the micas, chemical formulas were calculated using the following normalization procedure: **i**) OH contents were calculated on the basis of 11 oxygen per formula unit; **ii**) all Fe was assumed to be Fe^{2+}, **iii**) tetrahedral sites were filled with Si and Al to an occupancy of exactly 4; **iv**) remaining Al was assigned to octahedral sites together with divalent cations (except Ca^{2+}) and Ti, Cr, V and Li; **v**) interlayer sites were filled with Na, Ca and K. The phengitic component (% ph) is evaluated as a percentage of the ratio $^{[VI]}$(Fe+Mg+Ti+Mn)/ $^{[VI]}$(Fe+Mg+Ti+Mn+Al)). The results of these calculations are reported in the supplementary Appendix 1.

3.2. *Fluid inclusion studies*

Representative samples with respect to the continuous vein system emplacement described above were selected for a fluid inclusion study. It corresponds to (1) a fresh aplitic sill sampled away from muscovitization and quartz-veining (SG359a); (2) a N120°E intermediate vein also sampled away from muscovitization and quartz-veining (SG358); and (3) a mineralized striped foliation-vein exhibiting oblique elongate quartz grains (SH29). Fluid inclusions (FI) were analysed in doubly polished wafers 150 µm thick. All examined FI were hosted by quartz. In the mineralized vein, FI are associated with transparent quartz intergrown with ore minerals. FI are classified on the basis of their morphology at room temperature and chronology. They were considered as primary when; 1) they occurred in a crystal growth zone; 2) they occurred in an isolated cluster; 3) no relationship with microfractures was found. FI were considered as secondary when they lined up along planes. The Fluid Inclusion Assemblage (FIA) approach (Goldstein and Reynolds, 1994) was adopted. It consists of identifying a restricted zone of contemporaneous FI using petrographic criteria and to measure phase transition temperatures. A mean value (composition and density) is therefore assumed to represent a short time of fluid trapping at a given moment of system evolution. Values are given with standard deviation. A Linkam heating and freezing stage (LGCgE, Université Lille 1) was used for microthermometric measurements. The Linkam system consists of a TMS91 programmable temperature controller with an LNP2 pump and a THM600 heating and freezing stage attached to an Olympus BX40 microscope. The

stage was regularly calibrated with synthetic fluid inclusion standards (melting temperature of CO_2: -56.5°C; ice melting temperature: 0.0°C and critical homogenization temperature of water: +374.1°C). For measurements between 25°C and 100°C, the accuracy of the stage is ±0.2°C, whereas between 200° to 400°C, the accuracy is ±1.0°C. Salinities of inclusions were calculated from the ice melting temperature $Tm_{(ice)}$ in the H_2O-NaCl system (Bodnar et al., 1993). All Raman analyses were carried out on a Horiba JobinYvon HR 800 UV Raman spectrometer (Earth Sciences Department, Université Lille 1). Excitation was achieved using an ionized argon Lexel laser, tuned to 532 nm. Integration times typically ranged from 30 to 120 s. The Raman spectrometer was calibrated for determining the volatile content of the water phase (CO_2, CH_4, N_2 and H_2S) using the procedure described in Dubessy et al. (1989) and Burke (2001).

3.3. *Raman Spectroscopy of Carbonaceous Material (RSCM) geothermometry*

The geothermometry approach of Raman Spectroscopy of Carbonaceous Material (RSCM) is based on the quantitative estimation of the degree of structural transformation of Carbonaceous Material (CM), which has been proven as a reliable indicator for peak-temperatures (Beyssac et al., 2002; Lahfid et al., 2010). Because of the irreversible character of physio-chemical transformations, CM structure is therefore convenient for determining peak T-conditions (noted Tmax thereafter) even in strongly retrogressed metasedimentary rocks (Beyssac et al., 2002; Lahfid et al., 2010, Delchini et al., 2016). Tmax can be determined in the range of approximately 300 to 640°C with an accuracy of ±50°C related to the precision and the dispersion of petrological data used for the method calibration. Relative uncertainties on Tmax appear however much smaller, probably around 10 to 15°C and variations of that order of magnitude may be detected. Raman spectra were obtained using the Renishaw inVia Reflex system (BRGM- ISTO, Orléans). RSCM analyses were conducted on thin sections prepared on CM-rich metasediments cut in the structural X-Z plane (*i.e.*, orthogonal to foliation and parallel to lineation). To avoid defects on the CM related to thin-section preparation, analyses were all performed below the surface of the section by focusing the laser beam beneath a transparent crystal (*i.e.*, dominantly quartz, feldspar and phylosilicates).

3.4. *Geochronology*

U–Th–Pb geochronology on zircon was conducted by *in situ* laser ablation inductively coupled plasma-mass spectrometry (LA-ICP-MS) at Géosciences Rennes using an ESI NWR193UC excimer laser coupled to a 7700x quadripole Agilent ICP-MS. The ablated material was carried into helium and then mixed with nitrogen and argon, before injection into the plasma source. Ablation spot diameters of 25 to 44 μm with repetition rates of 4 Hz were used. More information about the analytical procedure can be found in Ballouard et al., (2015) and in the supplementary Appendix 2. Data were corrected for U–Pb and Th–Pb fractionation and for the mass bias by standard bracketing with repeated measurements of the GJ-1 zircon (Jackson et al., 2004). The dated sample was analysed together with the zircon standard Plešovice (337.13 ± 0.37 Ma: Sláma et al., 2008) to monitor the precision and accuracy of the analyses. Four analyses of this secondary standard yielded a Concordia age of 337.1 ± 1.2 Ma (MSWD = 0.5). Data reduction was carried out with the GLITTER® software package developed by the Macquarie Research Ltd. (Van Achterbergh et al., 2001). Concordia ages and diagrams were generated using Isoplot/Ex (Ludwig, 2001). All errors given in Appendix 3 are listed at one sigma, but where data are combined for regression analysis or to calculate weighted means, the final results are provided with 95% confidence limits.

4. Multistage vein formation within the Thaghassa area

An extensive field survey was carried out in order to complement the existing geological maps (Hawkins et al., 2001a, b). Results are shown in a new map (Fig. 3a), redrawn following field observations and satellite images analyses. Readers are referred to the existing maps (Benkirane, 1997; Hawkins et al., 2001a, 2001b; Hindermeyer et al.; 1977, Mrini, 1993) to appreciate the changes.

4.1. *Field relationships and deformation*

4.1.1. Structural analysis, distribution of metamorphic records and kinematics of the ductile deformation in the BICM rocks

Within the Boumalne inlier, Cryogenian metaturbiditic rocks that are dominated by sandstone and silty mudstone show finite strain markers including $S_{0\text{-}1}$ cleavage/foliation and associated L_1 stretching and mineral lineation. Both foliation and lineation were studied, but they remain difficult to observe except in the hornfels zone surrounding the Ikniwn granodiorite, including the Thaghassa prospect, where they are well developed.

Foliation is defined by a planar-linear fabric mainly formed by phyllosilicates (chlorite, sericite to biotite). They are generally parallel to each other whatever the lithology. The foliation and cleavage show a constant ENE strike and dip toward the NW (N075°E 60°N, Fig. 4a), except in fault drag area (*i.e.*, NW-SE strikes) or when refracted (NE-SW strikes). The orientation of the stretching lineations (Fig. 4b) also appear fairly constant with a rather low dispersion from NW-SE to N-S trending directions (average: N170°E 55°N), except in fault drag areas (*i.e.*, NE-SW trending direction). According to metamorphic zones and micro-structural analyses, one can define 3 tectono-metamorphic records in order of increasing grade: **i**) a chlorite zone, **ii**) an outer hornfels zone and **iii**) an inner hornfels zone.

i) The chlorite zone is observed in the central and northern part of the Boumalne inlier where metasedimentary rocks show no direct evidence for contact metamorphic effects (*e.g.*, absence of spotted zone, >>1500m from intrusive contact). Rocks are chiefly characterized by a schistose texture defining a coarse cleavage defining a $S_{0\text{-}1}$ foliation that usually lies parallel to the bedding, except when refraction occurs. The chlorite zone contains the following mineral assemblage: detrital and recrystallized quartz, plagioclase and K-feldspar grains. Metamorphism seems to have resulted in the growth of chlorite that occurs as tabular grains oriented within foliation with fine-grained white micas flakes (sericite). Chlorite is pale green or colourless and has the composition of the clinochlore end-member. Graphite may be common, but finely dispersed in the slaty matrix. Other minerals of minor and variable modal abundance include magnetite-hematite, rutile, titanite, zircon and apatite. Manganese-rich layers may also be observed within metamorphosed black shales. Lineation is extremely discrete and is defined by chlorite and sericite. S-C fabrics indicative of relative movement, parallel to the average lineation trending direction, of reverse sense top-to-the-south deformation are common in the Boumalne inlier and are in accordance with large-scale asymmetric folds. Indeed, shear bands define unambiguous south-verging noncoaxial shear criteria (Fig. 5a).

The Thaghassa area, which is the main focus of our study (Fig. 3), occurs within the well-developed contact metamorphic aureole caused by the Ikniwn intrusion within the Cryogenian turbidites. The aureole may be divided into two main zones.

ii) The outer hornfels zone consists of a spotted phyllite zone in which foliation and lineation are easily discernable (Fig. 5b). Rocks are made up of quartz, feldspar, muscovite, chlorite, biotite and small spots of retrogressed andalusite and/or cordierite. The latter occurs as undetermined ghost minerals in thin section, which are intensively transformed into fine grains of white micas (pinite), chlorite, K-feldspar and quartz with ilmenite, titanite and apatite accessory phases. However, scanning electron microscopy (SEM) has revealed relicts of cordierite. All samples also contain small amounts of graphite, rutile and magnetite-hematite. When iron oxides are absent, pyrrhotite, pyrite and chalcopyrite are observed as disseminated grains, particularly if quartz veins occur in the same area. Skarnoids may be inferred in the manganese-rich layers which are characterized by the presence of Mn-garnet (spessartine) with the following composition ($Alm_{20\%}$; $Grs_{1\%}$; $Maj_{1\%}$, $Prp_{5\%}$; $Sps_{73\%}$ - abbreviations of Whitney and Evans (2010)). In addition, in fine-grained calc-silicate rocks, hydro-grossular occurrence has been noted ($Adr_{8\%}$; $Alm_{2\%}$; $Grs_{86\%}$; $Sps_{4\%}$). Toward the intrusion, porphyroblasts of cordierite and/or andalusite become more abundant with biotite. Note that biotite has also undergone a fluid-assisted retrograde metamorphism as grains are frequently replaced by hydro-biotite. Large flakes of muscovite are frequently observed but post-date kinematic shear criteria (Fig. 5c). They will be considered below as poikilitic, post-foliation, muscovite. In the outer contact zone, the foliation is mostly characterized by biotite. Retrogressed cordierites spotted minerals define a well-expressed stretching and mineral lineation (Fig. 5b), which is only observed locally in metapelitic layers. Re-crystallization tails also consist of syn-kinematic biotites (Fig. 5c). By contrast, shear criteria are more ambiguous to interpret. Indeed, if such spots frequently define asymmetric deformation, accommodated by sigma-type porphyroblast systems (Passchier and Simpson, 1986), then both reverse and normal senses of shearing are observed with respect to the NW-SW to N-S lineation direction. Top-to-the-south and -south-east reverse sense of shearing are the more abundant features recorded in spotted minerals (Fig. 5c). Top-to-the-north, normal shearing are thus less common criteria related to such mineral spotting (Fig. 5d).

iii) The inner hornfels zone is highlighted by the development of metamorphic K-feldspar and by strongly indurated, maybe variably recrystallized, fine-grained dark hornfels and schists. The zone extends ~200 to 500m from the Ikniwn pluton contact. The principal minerals are K-feldspar, quartz and biotite (Fig. 5e, 5f). Graphite is not observed within the strongly indurated dark hornfels. Sulfides (pyrite and pyrrhotite) are common trace minerals. Poikilitic muscovite is often present as large post-kinematic flakes (Fig. 5e). Moreover, rocks displaying an overall appearance of metatexite migmatites have been observed in a few outcrops approximately 250m away from the Ikniwn intrusive contact (Fig. 5f). These areas are characterized by well-preserved, penetrative, ductile fabrics and also by numerous, mm–cm-scale, concordant, stromatic sheets of leucocratic quartzo-feldspathic structures that are interpreted as sills and tension gashes (see below). Tight and isoclinal folds are common in this facies (Fig. 6a)

In the inner hornfels zone, the foliation is mostly characterized by biotite, which also defines a mineral lineation. Kinematic indicators are scarce, but top-to-the-north east, normal-sense of shear, are solely observed. Though, top-to-the-north, normal, shear bands are also observed to be accommodated by the boudinage of competent layers, including contact metamorphic spots and leucocratic sheets.

4.1.2. Leucocratic quartzo-feldspathic, aplitic and pegmatitic stocks

An important stock of leucocratic, aplitic and pegmatitic structures is mostly emplaced between the Ikniwn contact and the transition between the outer and inner hornfels zones (Fig. 3b). These bodies occur under the form of rare leucocratic quartzo-feldspathic patches, bands and veinlets (1 cm maximum in width and 5 cm to 2 m in length) that are concordant or discordant with respect to the main foliation, and as sills and dykes (up to 1 m in width and ≤10 m in length) mostly parallel to the main foliation (Fig. 4c). Within the inner hornfels zone and very close to the contact with the Ikniwn granodiorite, metatexite migmatite rocks are darker and intensively affected and invaded by small-scale leucocratic quartzo-feldspathic bands that are mostly parallel to the foliation and correspond to stromatic textures (Fig. 6a, b). Likewise, numerous leucocratic dilatant veinlets observed in migmatites are frequently deformed (*i.e.*, folded; Fig. 6c) and are not connected to the stromatic bands. They are small in size (<10 cm) and show a thin selvedge of biotite around them. In detail, several observations allow to better constrain the structural controls of these magmatic features. The bands occur parallel to the $S_{0\text{-}1}$ foliation or as veinlets oriented N120-N150°E 80W corresponding to tension-gashes arranged following an "en-échelon" geometry and are consistent with dextral movement (Figs. 4c and 6a). In the vertical plane, boudinage is frequent and top-to-the-north, normal sense of shearing is common along the N-S trending direction. These leucocratic quartzo-feldspathic structures have a haplogranitic mineralogical composition with K-feldspar, plagioclase and quartz (Fig. 6d). Muscovite is common but tends to be late in the paragenesis (Fig. 6d). If one considers the rare patches, the bands and the related tension-gashes, all these structures may present a biotite-rich selvedge separating them from their host rocks (Fig. 6c).

Although there is no obvious textural difference with respect to grain size and mineralogy between the stromatic and aplitic structures, we define below aplite as sills or dykes that are >5 cm in width. Note that pegmatites have also been observed but remain scarce. Aplite sills are common structures observed a few tens of meters further north, away from the granodiorite contact and around the transition between the outer and inner hornfels zones. Therefore, they are absent or rare within migmatites where structures are frequently <5 cm in width. Aplite and pegmatite sills are also parallel to the major plane of anisotropy (Fig. 4c) and exhibit pull-apart geometries consistent with a dextral motion that is coeval with their formation (Fig. 6e). Aplite sills may also occur as boudin-like lenses within the foliation (Fig. 6f). In the vertical plane, parallel to the regional lineation, shearing and boudinage suggest a normal fault component. Note that rare dykes may also occur within the Ikniwn granodiorite; they still retain the constant ENE strike, but dip toward the south and the north (Fig. 4c).

Aplites are mostly formed by quartz, plagioclase, K-feldspar, muscovite and rare garnet (Fig. 6g). Garnet has an almandine composition ($Alm_{70.5\%}$; $Grs_{1.5\%}$; $Prp_{6\%}$; $Sps_{22\%}$). The larger dykes tend to contain more muscovite. Pegmatites yield a similar assemblage with the addition of zoned tourmaline and display some graphic intergrowths. Tourmaline blue cores have foitite compositions, whereas the brown rims are determined to be schorl.

Within the surrounding metasediments, the growth of poikilitic, post-foliation, muscovite (Fig. 5e) is mostly observed in the vicinity of the aplo-pegmatite system. It probably corresponds to a thermal effect due to the emplacement of this system. The narrow zone affected by this process defines a new aureole of contact metamorphism centred on the aplite and pegmatite sill system. Herein, grains can have different sizes and may show a preferred orientation suggesting top-to-the north, noncoaxial normal shearing.

4.1.3. Quartz-feldspar-apatite veins with intermediate composition

This first type of veins (vein is herein used for structures that differ from magmatic-related sills and veinlets) remains scarce. Such veins preferentially occur within the inner hornfels zone as N120°E trending regular veins (*i.e.*, oblique to the foliation) grouped within an "en-echelon" global geometry (Figs. 4d and 7a, b) or as foliation-parallel veins (Figs. 4d and 7c). They range from 1 to 5 cm in width and are ≤1 m in length. Quartz remains the most abundant mineral (Fig. 7c, d, e). In addition to quartz, they contain: feldspar (K-feldspar and plagioclase), apatite, scarce muscovite, tourmaline (dravite) and titanite (Fig. 7d, e). Because feldspar grains are euhedral and larger than those found within the host rocks, they cannot be interpreted as inclusions from the surrounding metagreywacke (Fig. 7d). Veins may be zoned and characterized by concentration of plagioclase, quartz, K-feldspar, apatite and titanite along their rims, with only quartz in the core (Fig. 7e).

4.1.4. Muscovite alteration halos

Muscovite alteration is mainly localized within the outer hornfels of the Ikniwn pluton, but close to the transition with inner hornfels. Such muscovitization develops a muscovite selvedge (Fig. 7f) and particularly affects the aplo-pegmatite intrusive bodies and their immediate host rocks (*i.e.*, hornfelsed rocks). Silicification is also a common process, so that alteration usually also forms adjacent to mineralized quartz veins (see below, Fig. 7g). The larger the aplo-pegmatite bodies are, the greater the muscovitization processes are advanced; this greatly affects the surrounding metasedimentary host rocks. Thus, the muscovite alteration is spatially associated with the N075°E trending direction (*i.e.*, the foliation and sills trending direction). Rutile and sulfides may also be observed as trace minerals in the alteration. As a consequence of such an alteration, earlier feldspar and muscovite (muscovite grains from aplo-pegmatite and poikilitic ones) are altered displaying recrystallization features, replaced by typical fibrous and radial muscovite grains from the alteration halo (Fig. 7g).

4.1.5. Striped foliation-veins

These veins represent the principal mineralization and constitute the main economic part of the deposits. They are common, in both the outer and inner hornfels zones (Fig. 3b), but larger economic ones are predominantly developed in the outer hornfels (Fig. 8a). They are mainly parallel to the $S_{0\text{-}1}$ foliation and thus trend E-NE (Figs. 4e and 8a). Cross-cutting relationships show that such structures systematically intersect both intermediate vein and aplo-pegmatite systems (Fig. 8b). Veins range in size from 5 to 50 cm in width and are ≤10 m in length (Fig. 8a). Macroscopically, the most common veins formed within the studied area are quartz-rich and exhibit a typical internal layering. Indeed, the veins always have a striped appearance, for example, exhibiting a well-defined internal layering (Fig. 8c). This internal layering is usually sub-parallel to the foliation. Since veins occur as sheets between the foliation, they can be compared to striped foliation-veins (*e.g.* Bons et al., 2012; Koehn and Passchier, 2000). Lineation/striae at a small angle (pitch of 20-30° NE) to the vein long axis has also been observed and measured.

Right-lateral kinematics is commonly observed along striped foliation-veins. Indeed, the best-expressed shear criteria are asymmetrical pull-apart (Fig. 8b) with an associated quartz vein system oriented N120°E to N150°E (Fig. 8d). In that case, the main striped vein array is interpreted as shearing veins whereas the associated vein system consists of tension gashes. Both vein types opened in response to an ESE-WNW shortening direction. Occasional N040-050°E trending, shorter and thinner segments were also observed with a striped appearance. These segments describe narrow zones of vein stepover, oblique to the foliation, thus defining sigmoidal structures. Such stepovers are also interpreted as shear veins in which the N050E segments correspond to the strongest deformation direction (see discussion).

From a mineralogical point of view, striped foliation-veins are mainly composed of quartz and white mica (sericite). Vein infillings are characterized by low sulfide content (<2%) with sulfides, sulfo-arsenides, arsenides, sulfosalts, electrum and cassiterite. Sulfide and arsenide assemblages are frequently replaced by supergene hematite-goethite mixture, scorodite and jarosite. Microstructural observations show typical characteristics of striped veins (Koehn and Passchier, 2000) with abundant, elongate shaped quartz (Fig. 9a). Numerous inclusion bands occur. They are parallel to the vein direction, wavy and could be replaced or reaffected by stylolite plans (Fig. 9b). Such bands essentially consist in foliated wall-rock particles (Fig. 9c). Neo-formed radial microlites of sericite are largely represented along these inclusion bands. They may also occur as overgrowths on earlier white mica of the surrounding rocks, particularly in the muscovite alteration halos (Fig. 9c). Note that muscovite displaying recrystallization features, but hosted by host rock fragments within striped foliation-veins, is typical from the alteration halos. Quartz textures are very irregular. Comb and sub-euhedral quartz co-exist with anhedral micro-grains (Fig. 9a, d). Elongated comb quartz crystals are either normal to the vein walls or oblique (Fig. 9a). Their growth is limited by the inclusion bands thus defining ribbons that give the striped appearance to the veining (Fig. 9a, b). The uniform grain size between two successive inclusion bands suggests that ribbon filling was achieved by unitaxial growth (Hilgers et al., 2001). This means that during ribbon opening, quartz grains

grew in the same direction from wall to wall, and during each growth increment. Because elongation direction and obliquity can be used as indicators of the dilatency direction, we can deduce that dextral shearing controlled the formation of the striped veins (Fig. 9a). The development of anhedral quartz micro-grains occur along alignments or trends parallel to the inclusion bands and vein rims (Fig. 9d). Along these zones, one can alternatively find large zones invaded by micro-grains (Fig. 9e), thin recrystallized fissures or clear zones that host large quartz grains (Fig. 9d). These characters strongly suggest that the formation of these micro-grain bands of quartz were the result of recrystallization processes associated with ongoing and progressive deformation. Unambiguous dextral shearing associated with the micro-grain band formation confirms this first assumption (Fig. 9e, f). The part of the striped foliation veins that trend N040-050°E also presents elongated, blocky quartz grains. The angle between the elongated grains and vein wall (<<45°) is lower than in the case of the N080°E striped veins and the quartz grains appear to be more elongated (Fig. 9g). Stylolitic plans are also present within this type of vein and are not especially localized along inclusion bands (Fig. 9g). Within N120°E tension gash veins, (Fig. 8d), texture consists of euhedral zoned comb quartz grains, frequently developed normal to the vein wall, or as geodic infilling (Fig. 9h).

4.1.6. Late events

Two additional, yet minor, structural and magmatic manifestations are recorded within the Thaghassa area. An important array of N150°E trending faults also affects the sector with a dextral apparent displacement. If the aplo-pegmatite systems, striped foliation-veins and metasediment layers are curved in the vicinity of the fault, while dacite, andesite and dolerite dykes do not appear to be affected (Figs. 3b and 4). Field relationships are clear because all these dykes are not displaced by the dextral offset of the faults, even if slight recurrent faulting may be observed with displacement (Fig. 3b).

4.2. *Mineral chemistry and related geothermometers*

4.2.1. White mica compositions

All the white micas described below are classified as muscovite according to Tischendorf et al. (2004). Data herein presented as a graphical presentation illustrating the dioctahedral substitutions and their deviations to trioctahedral micas (Guidotti, 1984) allows the determination of three types of muscovite illustrating the magmatic-hydrothermal transition (Fig. 10a):

I) Muscovite from aplo-pegmatites structures, from the intermediate veins as well as the post-foliation poikilitic ones that ranges between $2.72 \leq R^{3+}_{total} \leq 2.99$ a.p.f.u[1]. and $0.02 \leq Fe+Mg+Ti+(Si-3) \leq 0.31$ a.p.f.u;

II) Muscovite from the alteration halos that ranges between $2.61 \leq R^{3+}_{total} \leq 2.83$ a.p.f.u. and $0.2 \leq Fe+Mg+Ti+(Si-3) \leq 0.45$ a.p.f.u;

[1] a.p.f.u.: atom par formula unit

III) Neo-formed microlites of sericite from striped foliation veins that range between $2.41 \leq R^{3+}_{total} \leq 2.57$ a.p.f.u. and $0.52 \leq Fe+Mg+Ti+(Si-3) \leq 0.67$ a.p.f.u.

The main characteristics of these three types of muscovite are as follows. Muscovite I has a chemical composition close to theoretical muscovite (Fig. 10a). Grains show an increasing phengitic component with average values of 18.75, 20.76, 26.46 and 29.59% considering aplite sills, pegmatites, poikilitic muscovite and those from intermediate veins, respectively. Likewise, type I muscovite is the most enriched in Al with an average amount ranging between 35.47 and 36.37 wt%. Fluorine contents range between 0 and 0.74 wt%. The average values show that aplite, pegmatite and aureole micas have similar contents (0.12 to 0.15 wt% F). Those from intermediate veins are slightly enriched in F with an average of 0.25 wt%. Type II muscovite is characterized by higher phengitic component (ave: 39.72%), whereas the average Al content decreases at 32.88 wt%. These types of muscovite show the lowest fluorine contents with an average of 0.07 wt%, but also the greatest variability (*i.e.*, from 0 to 0.19). Type III muscovite or sericite corresponds to neo-formed fine-grained sericites that are observed along the inclusion trends within striped foliation-veins. They have the highest phengitic component with an average of 64.63 wt% and the lowest content in Al with an average content of 31.35 wt%. Fluorine is abundant in this group as suggested by the average F content (0.33 wt%).

The variation of Al content in each type of muscovite may be charge balanced by the phengite-like substitutions. If such exchanges constrain muscovite to mainly preserve their dioctahedral feature (Guidotti, 1984), one can see a slight deviation towards the trioctahedral structure as illustrated in Fig. 10a for muscovite having higher phengitic components. Such a deviation is in particular led by: $^{[6]}(Mg^{2+}, Mn^{2+}, Fe^{2+})\ ^{[6]}(Ti^{4+}, \square)_{-1}$, with ($\square$) as vacancy.

The geothermometer of Monier and Robert (1986) is based on the behavior of the solid-solution domains of dioctahedral stable elements from 300 to 650°C and 50 to 300 MPa in the K_2O-MgO-Al_2O_3-SiO_2-H_2O-(HF) system (Robert, pers. comm.). Most of the muscovite I compositions lie inside the domain of solid solution stable between 500 and 650°C (Fig. 10b). Note that muscovite collected within intermediate quartz – feldspar veins yield maximum temperatures bracketed between 500 and 600°C. Type 2 muscovites from the alteration halos gives temperatures bracketed between 400 and more than 600°C, similar to sericites from striped foliation veins (type III). However, type III muscovite clearly shows a shift toward the phengitic component suggesting a lower temperature of formation than the type II variety.

4.2.2. Sulphide composition

The main Au-Ag mineralization and associated base-metal sulfides are observed within the striped foliation veins and related tension gashes, but also within hornfelsed host rocks. Within striped foliation-veins, sulfides are located either between comb and blocky quartz grains or disseminated within elongate quartz as small micrometric inclusions (≤ 100 µm). Mineralization formation occurs in two stages: **i**) an earlier stage consisting of dominant base metal ore with Sn; **ii**) a later Ag-Au-Cu-As stage paragenesis

filling micro-cracks in the core of primary sulphides. The dominant mineralogy consists of pyrite and arsenopyrite. Both minerals occur as filling of open space and/or disseminated within quartz veins or host rocks. EPMA data are given in supplementary Appendix 1.

Pyrite occurs in the form of sub-euhedral grains that exhibit growth bands revealed by etching with HNO_3 and back-scattered SEM observations. It shows that the pyrite is chemically zoned, thus allowing the distinction of polyphased growths (Fig. 11a). Pyrite cores show homogenous compositions characterized by minor amounts of arsenic (average amount of As is close to 0.71 wt%). Conversely, the external part of the pyrite grains is characterized by a succession of As-rich pyrite bands (from 1.21 to 2.64 wt% As, with an average value of 2.01 wt% As) and As-depleted bands (with values below the detection limit to 0.16 wt% As and an average of 0,08 wt% As). As well, significant values of Ni (max 0.61 wt% Ni) have been detected within the As-rich pyrite bands. All pyrite analyses show systematic amounts of Pb that can be correlated with the presence of numerous micrometric to sub-microscopic inclusions of galena (Fig. 11b). Occasional concentrations of Bi and Co have also been detected. *Pyrrhotite* is present as inclusions within all the generations of pyrite. Sub-euhedral *arsenopyrite* is observed only within the external pyrite zones (Fig. 11a), where pyrite contains significant amounts of As. Two types are distinguished (Fig 11c): the former (type 1) is depleted in As (46.24 wt% As), whereas the second one (type 2) is enriched in As (47.58 wt% As) and encapsulates the type 1 (Fig. 11c) or fills micro-cracks along crystallographic orientations. The structural formula calculated on the basis of a total of three atoms is $Fe_{0,99}(As_{0,92}Sb_{0,01})S_{1,07}$ for arsenopyrite 1 and $(Fe_{0,98}Co_{0.01})(As_{1.04}Sb_{0,01})S_{0.95}$ for arsenopyrite 2. Arsenopyrite 2 presents significant amounts of Ni (average 0.23 wt%) and Co (average 0.28 wt%). Traces of Pb have also been systematically detected within arsenopyrite 1 and correspond to micrometric inclusions of galena (Fig 11c). Numerous other sulphides also compose the ore paragenesis. *Sphalerite* is abundant and systematically contains numerous micro-inclusions of *chalcopyrite*. Iron contents in sphalerite range between 6.52 and 8.95 wt% with average concentrations of 0.25 wt% Cu, 0.50 wt% Mn and 0.29 wt% Cd, respectively. *Loellingite* is associated with arsenopyrite 2 and shows a mean concentration of 1.37 wt% Ni and 0.35 wt% Co, respectively. *Tetrahedrite* averages 12.10 wt % Ag, with a range of 11.91-12.38 wt% and is associated with sphalerite and pyrite 2. *Cassiterite* is related to chalcopyrite and appears as inclusions within arsenopyrite 2 (Fig. 11d). Both are considered as prior to arsenopyrite 2. The economic minerals, *i.e.*, Au- and Ag-bearing ones, occur late in micro-cracks within the main sulphides (Fig. 11e, f). The paragenesis contains chalcopyrite, *freibergite*, *electrum*, and arsenopyrite *2*. Freibergite averages 21.46 wt% Ag and 1.49 wt% Zn according to the structural formula $(Ag_{3.6},Cu_6,Fe_2,Zn_{0.4})\Sigma_{12}\,(Sb_{3.9},As_{0.16})\Sigma_{4.06}\,S_{12.8}$ (Table 3). Electrum is Ag-rich.

According to studies of Kretschmar and Scott (1976) and Sharp et al. (1985), the use of the arsenopyrite chemical compositions to assess ore formation temperatures may be considered. However, traces of Co, Ni, or Sb may disturb the use of the arsenopyrite geothermometer when correlations between As–Co, As–Ni and As–Sb are evident. As explain above, our analyses reveal the presence of significant amounts of Co, Sb and Ni within the two generations of arsenopyrite (*e.g.*, Co: 0 to 0.28 wt% for arsenopyrite 1 and 0

to 0.75 wt% for arsenopyrite 2; Sb: 0.15 to 1.2 wt% for arsenopyrite 1 and 0.13 to 1.20 wt% for arsenopyrite 2; Ni: 0 to 0.43 wt% for arsenopyrite 1 and 0 to 1.06 wt% for arsenopyrite 2). According to the limitations discussed earlier, arsenopyrite 1 cannot be evaluated using the geothermometer. Because no significant correlation between As and Sb-Co and Ni has been observed, and taking into account the equilibrium between loellingite and arsenopyrite, a temperature of crystallization comprised between 350 and 450°C for the arsenopyrite 2 with a sulphur fugacity (fS_2) ranging between 10^{-7} and 10^{-11} atm is proposed, in accordance with the FeS content of sphalerite (Barton and Toulmin, 1964).

4.3. *Preliminary fluid inclusion petrographic and microthermometric studies*

Microthermometric experiments are discussed in the context of analysing FIA in the three examined quartz samples. All analysed FI belong to a general H_2O-CH_4-N_2-CO_2 ± NaCl fluid system with variable composition. On the basis of natural sample, chronology and phase proportions at room temperature, 4 types of FI have been identified:

Type A inclusions are only observed in the aplite sample. They are less than 5 µm in size and commonly occur as isolated clusters. They are therefore classified as primary. The vapour phase represents more than 90% of the FI volume. In the favourable cases where a liquid rim is observable, ice melting temperatures ($Tm_{(ice)}$) were measured near -5.7/-5.6°C, corresponding to a salinity range of 8.7 to 8.8 wt.% eq. NaCl. FI homogenize into the vapour phase ($Th_{(v)}$), mainly in the interval 327°C to 373°C (Fig. 13a). FI may be N_2 or CH_4 dominant or a mixture of CH_4 and CO_2 (Fig. 13b). Raman spectrometry reveals traces of graphite within CH_4-rich FI.

Type B FI have been observed in the intermediate vein where they are considered as primary. They have also been observed within the aplite sample, but in that case, they are classified as secondary. FI are between 2 and 10 µm in size and contain two phase (LV) inclusions with extremely variable proportions between 10 and 90%, but mostly >50%. Vapour consists of either CH_4-N_2 or CH_4-CO_2. Note that CO_2-rich fluid inclusions remain scarce (Fig. 13b). Raman spectrometry shows evidence of graphite in the vapour-rich FI. $Tm_{(ice)}$ mostly occurred between -2.7 and 0°C thus indicating low salinities of 0.9 to 4.5 wt.% eq. NaCl. FI homogenize into the liquid phase in the interval 230°C to 380°C, and in the interval 350-410°C to the vapour phase (Fig. 13a).

Type C inclusions have been solely observed in the striped foliation-vein sample. They are ~5µm in size and are distributed in successive growth zones, indicating a primary origin or along or along microcracks. They are also two-phase (LV) inclusions, with a vapour of about 20% volume. The volatile content varies considerably inside a given crystal growth zone or cluster. Type C FI have a vapour dominated by CO_2 with minor proportion of CH_4 (Fig. 13b), whereas they are pure CH_4 only when classified as pseudo-secondary or secondary. Raman spectrometry revealed the presence of albite, calcite and K-feldspar within primary inclusions. $Tm_{(ice)}$ lie between -7.8 and 0°C, corresponding to low to medium salinity (interval 0 to 11.5 wt.% eq. NaCl). Primary type C FI homogenize into the liquid phase between 220 and 410°C (Fig. 13a). Pseudosecondary / secondary type C inclusions have similarly a Th range between 190

and 390°C, but by contrast, they show $Tm_{(ice)}$ between -26 and -5°C thus suggesting higher salinities (between 7.9 and >23 wt.% eq. NaCl).

Type D embraces two phase FI homogenizing into the liquid phase. They have only been observed in intermediate and striped foliation-veins. Their chronological position is systematically secondary. These inclusions have a composition in the H_2O-salt system with a low to high salinity (maximum 27 weight % NaCl equivalent). Their Th are bracketed between 170 and 260°C (Fig. 13a). Decrepitation during heating stages is a very common feature.

4.4. *RSCM T results*

The data set consists of 6 CM-bearing samples collected within pelitic layers of the metaturbiditic rocks and are regularly distributed along a N-S transect within the Boumalne basin inlier (Fig. 14). At least 10 spectra were recorded for each sample to bring out and possibly smooth out the inner structural heterogeneity of CM within samples. Internal dispersion of RSCM data presents generally unimodal Tmax distributions and ranges from 7 to 23°C. From north to south, RSCM temperatures show high temperature gradients ranging from 500 to more than 640°C. The highest temperatures (>640°C) have been observed close to the Ikniwn granodiorite pluton within the spotted-hornfels zone at maximum 1km from the intrusion.

4.5. *New geochronological data*

Sixteen analyses have been performed on 7 zircon grains from the Ikniwn granodiorite intrusion. The grain sizes range between 20 and 250 µm. They are mainly coarse grains, with shapes belonging to the S15-P3 to AB5-A of the Pupin (1980) classification, which is in agreement with the host lithology and correspond to temperature of crystallization in the range of 750 to 550°C. All zircon grains display typical magmatic oscillatory zoning. Average U, Pb and Th concentrations are 247 ppm, 22 ppm and 78 ppm, respectively (supplementary Appendix 2). U/Th ratio are homogeneous with an average value at 0.3. Most of the analyses are concordant or with a slight common Pb contribution and/or radiogenic Pb loss. The 9 analyses that are more than 98% concordant (Appendix 3 in electronic supplementary data) yield a Concordia age of 563.5 ± 6.3 Ma (MSWD=2.1, Fig. 15). If we take the 16 analyses, the weighted average $^{206}Pb/^{238}U$ date is equivalent within error at 557.3 ± 5.8 Ma (MSWD=3). This date of 563.5 ± 6.3 Ma is interpreted as the emplacement age for the Ikniwn granodiorite intrusion.

5. Interpretations and discussion

The above observations document the occurrence and formation of a hornfels-hosted sheeted quartz vein system. The discussion below focuses on: **i**) the earlier deformation of country rocks, **ii**) the continuum between magmatic and hydrothermal processes including source reservoirs, **iii**) the structural control of striped quartz vein emplacement and **iv**) the regional implications.

5.1. *A top-to-the-south asymmetry and syn-kinematic pluton emplacement*

The BICM rocks are herein exposed as a NW- to NNW-dipping folded sequence as explained by Benkirane (1987). They present a NW-SE to N-S stretching direction and highlight a top-to-the-south deformation in a ductile regime (Fig. 16). Although previous studies reported low-grade metamorphic conditions, we assume herein that deformation was accompanied, in the whole Boumalne inlier, by coeval gradients in upper greenschist- to lower amphibolite-facies conditions (500<T°C<550) as suggested by the RSCM Tmax method. This analysis was strengthened by the recognition of syntectonic minerals, such as clinochlore and sericite. Amphibole, biotite and garnet previously described by Benziane (2007) may also be indicators of higher T metamorphic conditions. However, it is not entirely clear whether such a high T gradient is due to a regional or a contact metamorphism. Note that if the metamorphism is due to a thermal aureole, then the Ikniwn granodiorite should have gentle contacts toward the north with its host rocks. This may thus explain the wide extension (up to 6 km and perhaps more) of the metamorphic aureole as described by Hindermeyer (1953). We therefore suggest a syn-tectonic emplacement for the Ikniwn granodiorite as proposed by Errami and Olivier (2012), as this explains the high T contact metamorphic spots (*i.e.*, cordierite and andalusite) associated with asymmetric features dominated by top-to-the-south deformation in the southern part of the Boumalne basin inlier.

5.2. *A magmatic to hydrothermal transition at the origin of the Thaghassa IRG deposit*

Based on our new structural and petrographic observations, fluid inclusion studies, geothermometry and geochronological constraints on the studied area, we discuss herein the role of the last main tectonomagmatic event, which occurs from plastic to brittle conditions and highlights a progressive evolution from the magmatic to the hydrothermal stages.

5.2.1. In situ anatexis of metasediments and fluid releasing

Unlike the top-to-the-south deformation described above, this tectonomagmatic event has been observed only in the vicinity of the Ikniwn intrusion, where the former top-to-the-south imprints have been, locally, completely erased and transposed. In such a setting, the origin of stromatic texture and leucocratic quartzo-feldspathic concordant bands and veinlets is herein interpreted as having an anatectic origin. Indeed, taking into consideration existing field observations, mineral textures and RSCM Tmax geothermometry, we suggest that metagreywackes and metapelites were affected by a low P and high T metamorphic gradient that reaches its paroxysm during anatexis within the Ikniwn granodiorite aureole. The Ikniwn granodiorite provided the heat; this intrusion and the metasediments that underwent devolatilization, probably released fluids, both resulting in partial melting.

Similar interpretations have been made for different metamorphic aureoles where migmatites and/or leucocratic segregations are observed (Finger and Clements, 1995; Pattison and Debuhr, 2015; Pattison and Harte, 1988; Symmes and Ferry, 1995). Moreover, experimental studies have shown that at a pressure of 200 to 400 MPa, partial melting of metapelites under H_2O-saturated conditions begins between 625

and 750°C and generates haplogranitic compositions (Genier et al., 2008; Icenhower and London, 1995; Pattison and Harte, 1988). We herein propose that the stromatic features belong to a metatexite migmatite zone, which exclusively occur within the fine-grained dark inner hornfels zone, less than 300m away from the contact with the Ikniwn pluton contact, resulting from partial melting of metaturbidites (>640°C) at or near H_2O-saturated condition.

In addition to quartz and feldspar observed in leucosomes, biotite and muscovite are the typical index minerals of this stage. Muscovite occurs both as a contact metamorphic mineral around aplitic injections and as a magmatic mineral within sills. Because biotite shows similar features (*i.e.:* oriented habit, colour, size and is not poikilitic) when observed in the outer and the inner hornfels (within the foliation or around the metamorphic spots), as well as in the metatexite zones, it is thus interpreted as metamorphic in origin. Biotite from the selvedge observed at the rim of leucocratic quartzo-feldspathic veins also displays these similar features and is interpreted as a melanocratic residuum concentrated after the extraction of a partial melt. Biotite, which is frequently enriched in such rocks and mostly occurs in melanosomes, is interpreted as a residual metamorphic fraction and does not correspond to a potassic alteration. Thus, the texture of metatexites, the haplogranitic mineralogical composition of the leucocratic quartzo-feldspathic bodies, their patches, band or veinlet structures and the recurring observations of thin selvedge of biotite at their rims strongly argue for an anatectic origin (Johannes, 1983; McLellan, 1983; Sawyer, 2008). We further assume that most products of crystallization observed in the field may be classified as in-source leucosome, although *in situ* leucosomes may sometimes be expected (Oliver and Barr, 1997; Sawyer, 2008). However, most aplite and pegmatite sills localized at the transition between the inner and outer hornfels zones, correspond to the vertical extent above the stromatic zone (Fig. 16). Note that we do not preclude that some aplites or pegmatites (*i.e.*, the ones hosted within the granodiorite and perhaps the larger ones) may be related to the fractionation of the closely connected Ikniwn granodiorite. Because all these observations have been made in a large proportion of the studied area, we suggest that such a partial melting process is a key parameter at the origin of the ore-forming processes.

5.2.2. The metamorphic versus magmatic origin of ore-forming fluids

The common source of debate about gold deposits in plutonic and metamorphic environments is whether the fluids that have contributed to the ore formation are magmatic and (or) metamorphic in origin. Models suggest that during prograde metamorphism, the leakage of fluids occurs at a very low rate from plastic rocks at lithostatic pore fluid pressure (P_f) toward the overlying hydrostatic P_f in brittle systems, because of the very low porosity and permeability of recrystallizing rocks (Fournier, 1999; Yardley, 2005). Such metamorphic fluids are thus unlikely to form an ore deposit. However, faster dehydration can be catalyzed by a significant magmatic input that introduces additional heat that can produce, at depth, metal-rich fluids that will flow upward, assisted by P_f fluctuations in fault-valve systems, to form ore deposits during cooling (Sibson et al., 1988; Yardley and Cleverley, 2015).

The record of a continuous and progressive vein system formation from metamorphic-magmatic to hydrothermal conditions represents an obvious criterion for a metamorphic-magmatic-hydrothermal connection closely linked with ore formation processes. Similar cases are very scarcely described in the literature and only a few papers very concisely underlined the evolution, in space and time, from aplo-pegmatitic to gold-bearing quartz veins (*e.g.*, Baker and Lang, 2001; Kontak and Kyser, 2011; Mair et al., 2006; Mustard, 2001; Thorne et al., 2008). In our case, the lack of absolute geochronological constraints can question the continuous formation of all the vein and sill structures. However, the sill and vein system must have been emplaced between the Ikniwn granodiorite intrusion (*i.e.*, the 558 to 570 Ma interval) and the various acid and intermediate volcanic dykes (Fig. 3b), which crosscut the mineralized veins, but were emplaced prior the Isk n'Allah granite emplacement (the 551 to 559 Ma interval). Thus, their intimate spatial relationships, their parallelism and their formation during the same tectonic event represent sufficient arguments to discuss the existence of a link between magmatism and hydrothermal activity. Thus, the devolatilization of metasediments and the underlying crystallizing Ikniwn granodiorite (overburden pressure of ~100 to 200 MPa and 750 to 800°C; recalculated from Chaker (1997) data using the Schmidt (1992) and Ridolfi et al. (2010) thermobarometric formulations) may provide fluids and heat into the overlying metaturbidites resulting in a localized partial melting.

Samples collected in a selected aplitic sill, an intermediate vein and a mineralized striped foliation-vein revealed 4 distinct fluid types:

- (A) a high T, low density and low to intermediate salinity (<9 wt.% equivalent NaCl) fluid dominated by N_2 or CH_4, solely observed in the aplitic sill;
- (B) a high T fluid with various density, low salinity (<4.5 wt.% eq. NaCl) and presence of CH_4-N_2 or CH_4-CO_2, in the intermediate vein;
- (C) a high to medium temperature of higher density fluid, with low to intermediate salinity (<11.5 wt.% eq. NaCl), with presence of CO_2 and traces of CH_4, in the observed in the striped foliation-vein;
- and (D) a significantly lower T, volatile-free fluid with higher salinity (until ~27 wt.% eq. NaCl) trapped in secondary FI in both the intermediate and striped foliation-veins. According to its chronological position, fluid chemistry and temperature, this fluid is probably disconnected from previous fluid types.

We therefore interpret the successive fluids as recording the evolution of a main aquo-carbonic fluid undergoing a density increase from aplite to intermediate vein and finally, to the striped foliation vein. If one considers the transition between magmatic and hydrothermal processes, such an increase may be interpreted as a condensation process in response to a temperature drop in the system. The nature of the volatile components clearly appears to evolve from N_2-CH_4 in earlier magma-related fluids to CH_4-CO_2 in the late hydrothermal striped quartz-veins. The initial primacy of N_2 and CH_4 suggests a reducing character of the fluids and an origin directly related to partial melting of country rocks. Indeed, as N_2 and CH_4 solubilities in melts are very small, even in reduced conditions and much lower than those of CO_2

and H_2O, it follows that both species will exsolve early (Ardia et al., 2013; Holtz et al., 1992; Jakobsson and Holloway, 1986; Libourel et al., 2003; Lowenstern, 2001). Consequently, under reducing conditions, the most likely melting reaction involves quartz, feldspar, biotite and graphite with a possible source of fluid either from the crystallizing pluton or the metamorphic devolatilization of country rocks, or from both of them, such as:

$$C+2H_2O \Leftrightarrow CH_4 + O_2 \text{ (1)},$$

$$\text{and, } Fsp+Qz+H_2O\pm Al_2SiO_5\pm Crd\pm Bt\pm C \Rightarrow L_{(melt)} + CH_{4(v)} + N_{2(v)} \text{ (2)}.$$

In such a setting, devolatilization processes of the country rocks release fluids enriched in N_2 and CH_4 during contact metamorphism and then anatexis (reaction 2). This thus explains the frequent observations of graphite traces in type A and B fluid inclusions.

While considering the magmatic-hydrothermal transition, the increasing concentrations in CO_2, from intermediate to striped foliation-veins, seems clearly associated with the progressive shift toward increasing hydrothermal conditions. Because close relationships between low and high density FI have not been seen, effervescence processes are not envisaged to explain the CO_2 enrichment. Likewise, CO_2 could be exsolved from melt (anatectic melt and (or) granodioritic melt) by first or secondary boiling, but the absence of CO_2 in FI from the aplite precludes the eventuality of an early CO_2 saturation in melts. So, CO_2 should have a metamorphic (devolatilization) or a hydrothermal origin. In both cases, its formation may be buffered by the following reactions:

$$C + 2H_2O \Leftrightarrow CO_2 + 2H_2 \text{ (3)},$$

$$\text{and, } CH_4 + 2O_2 \Leftrightarrow CO_2 + 2H_2O \text{ (4)}.$$

The involvement of multiple reservoirs, from both magmatic and non-magmatic origins, has been already demonstrated in order to explain the genesis of intrusion-related gold deposit mineralization by Kontak and Kyser (2011).

At last, secondary type D fluid, characterized by a highly variable salinity, could be compared with the Ag-bearing brines described in the giant Imiter silver deposit, situated 15 km to the NE (Essaraj et al., 2016; Hulin et al., 2013).

5.2.3. A strain regime change leading to the emplacement of the Thaghassa IRG deposit

Following the top-to-the-south compressive deformation, our study shows that the formation of magmatic and hydrothermal veins of the Thaghassa area is clearly related to a top-to-the-north asymmetry leading to a normal-sense of shearing with a dextral component (Fig. 5d). Indeed, the formation of stromatic features and aplo-pegmatitic sills are both associated with a strain regime change associated with top-to-the-north normal shearing and ENE-WSW horizontal dextral shearing as illustrated by "en-échelon" tension gashes and pull-apart geometry (Fig. 6a, b, f), as well as the later continuous emplacement of the sheeted striped foliation-veins (Fig. 16). Thus, the formation of the Thaghassa IRG deposit has been integrated within a three stage schematic evolution in which all the herein described features can be formed in response to an ESE-WNW direction of shortening (Fig. 17).

i) During the first stage, leucocratic bands, aplite and pegmatite sills are emplaced coevally in response to partial melting of the BICM rocks and because of the effects of emplacement of the Ikniwn batholith. As discussed above, it is possible that some aplites or pegmatites may be related to the fractionation of the closely connected granodiorite. Most sills occur parallel to the cleavage planes (Fig. 17a) certainly because this plane is preferentially reactivated during shearing. Few examples of magmatic features (pull-apart geometries, boudinage and tension gashes) showing ENE-WSW dextral shearing with normal components (Fig. 6a, b, e, f) also demonstrate the same structural control that also argue for a coeval emplacement of these magmatic structures (Fig. 16) at a temperature close to 500 to 650°C (Fig. 10b). During this first stage, high T fluids with low density dominated by N_2 or CH_4 and low to intermediate salinity are exsolved (type A FI).

ii) The following stage (Fig. 17b) is linked to the emplacement of the intermediate veins, locally parallel to the cleavage planes (Fig. 7c), but more commonly as N120°E regular planes (Figs. 7a and 16). The second type corresponds to veins formed as tension gashes, *i.e.*, parallel to the main shortening direction (Fig. 17b). The association of quartz with feldspar and muscovite at the rim and the chemical similarity of these white micas with those from the aplo-pegmatite sills, questions the nature of these intermediate veins. Considering the muscovite geothermometer that suggests a maximum temperature of formation close to 500°C, these veins may indicate the persistence of a magmatic character, at least at the beginning of their formation. We assume that these veins are intermediate because their formation is situated between the magmatic (aplite and pegmatite) and the hydrothermal quartz-bearing vein systems, thus highlighting a transition between magmatic and hydrothermal processes. Note that earlier leucocratic tension gashes are more deformed and curved in response to the ongoing deformation (Fig. 17b). During this second stage, high T fluids of various density with either CH_4-N_2 or CH_4-CO_2 and low salinity are invoked.

iii) The final stage is related to the muscovite alteration halos and the formation of the main mineralized striped foliation-veins (Fig. 16). The formation of the muscovite alteration can be thus described by the following reactions that consume feldspars from both aplites and host-rock by hydrolysis, to give muscovite:

$$3KAlSi_3O_8 + 2HCl \Leftrightarrow KAl_3Si_3O_{10}(OH)_2 + 6SiO_2 + 2KCl \quad (5), \text{ and}$$

$$3NaAlSi_3O_8 + 2HCl + KCl \Leftrightarrow KAl_3Si_3O_{10}(OH)_2 + 6SiO_2 + 3NaCl \quad (6).$$

Because fluids are saturated with SiO_2, this may explain why striped quartz-veins formed at the core of these muscovite alteration halos.

Their opening direction and sense of shearing are determined by the quartz grain obliquity (Figs. 9a and 17c) within the main segments of the veins (Cox, 1987; Cox and Etheridge, 1983; Hilgers et al., 2001). An ENE-WSW dextral kinematic is proposed, although the lower pitch of the lineation/striae includes a slight vertical component. Taken together, the striped aspect of the veins, the presence of undulatory extinction and the development of sub-grains of quartz (Fig. 10e, f) suggest that episodic shearing or faulting, and incremental opening of these veins must have occurred under brittle-ductile conditions. The

existence of tension gash veins is an additional argument for the persistence of the ESE-WNW shortening direction during this stage (Figs. 16 and 17c). Stylolites parallel to the vein wall within N040-050°E trending segments of the veins can result from this direction of shortening (Fig. 17c). Mineralization occurs in two main steps: an earlier one consisting of base metal sulfides and Sn and a later step of Ag-Au-Cu-As. The association of arsenopyrite and loellingite associated with the Ag-Au-Cu-As paragenesis yields a maximum temperature of formation of 350 to 450°C for this stage, consistent with the one obtained with the muscovite thermometer applied on radial neo-form muscovite of the striped veins. In that case, fluids invoked at the origin of the ore deposition have medium to high temperature (220<Th°C<410), a low to intermediate salinity (<11.5 wt.% eq. NaCl) with presence of CO_2 and traces of CH_4.

5.2.4. Parameters controlling quartz, muscovite and sulfide precipitations

The progressive increase of quartz amount from the intermediate to the striped foliation-vein stages is the result of fluctuations in fluid density, salinity and temperature and hydrostatic P_f (Fournier, 1999). So, the quartz solubility decreases from the higher P_f to the lower P_f and for T>100°C. Note that salinity may significantly enhanced the quartz solubility. Also at constant T, quartz solubility shows a decreasing trend although, a domain of prograde solubility occurs, upon cooling, for P_f below 80 MPa and temperatures between 350 and 550°C because of the change of the fluid density (from vapor-like to liquid-like fluid; Fournier, 1999; Kouzmanov and Pokrovsky, 2012). For example, at about 50 to 60 MPa and for temperature of *ca.* 550°C, the solubility of quartz increases again to reach a maximum at 450 to 350°C for constant P_f, before strongly decreasing again. Thus, major perturbing events such as intermittent seismic slips observed in the striped foliation-veins will cause abrupt reductions in P_f and thus quartz precipitation as explained in the fault-valve model of Sibson et al., (1988). The incremental formation of striped foliation-veins herein compared to shear veins, is explained first by progressive P_f overpressure exceeding the lithostatic load that causes failure in zones of weakness (*i.e.*, the wall rocks of the veins) and an increase in permeability in the fracture. Then, the hydrothermal discharge occurs all along the fracture causing an abrupt drop in P_f. Quartz precipitation occurs there in the 450 to 350°C window aided by the significant reduction of P_f and will continue until the ribbon (fracture) is sealed. At last, P_f will progressively increase again leading to the development of cyclic fluid-activated seismic valves.

From a chemical viewpoint, each type of muscovite is constrained by important phengite-like substitutions that show an increase of these exchanges with respect to time and decreasing temperature. The increase of the phengitic component correlates with a slight deviation of these dioctahedral micas that tend to incorporate a trioctahedral component. Moreover, the fluorine content of each muscovite type suggests a consistent increasing trend from the magmatic (avg. 0.12-0.15 wt %, Appendix 1), intermediate (avg. 0.25 wt %), to the hydrothermal stages (avg. 0.33 wt %). The only issue is the low fluorine content (avg. 0.07 wt %) for the muscovite from the alteration halos. An explanation may be that, during the alteration of the aplites and possibly of the surrounding host rocks, earlier magmatic F-bearing

muscovite was leached and fluorine was concentrated at the core of the alteration halo within quartz veins. This thus explains the highest fluorine enrichment of muscovite from the striped quartz-veins. Nevertheless, the chemical features of all the muscovite types stress the continuum between magmatic, magmatic-hydrothermal and hydrothermal stages. Taking into account that such an alteration assemblage comprising mainly muscovite, quartz with scarce rutile and sulphides and the feldspar hydrolysis given by reactions (5) and (6), such a muscovitization may possibly correspond to a greisen-like alteration, despite the lack of evidence for significant concentration in other, untested, incompatible elements such as Li, Rb, Ta and Cs. It is apparent that hydrolysis reactions may be effective mechanisms for ore deposition, as it also leads to a pH increase in the fluid.

Indeed, the acidity, fO_2-fS_2, but also the temperature and salinity of the fluids, with the nature of the metal-transporting complexes are key parameters controlling sulphide and precious metal precipitation (Fontboté et al., 2017; Yardley, 2005). At Thaghassa, FI study indicates that mineralized fluids (Type C) have high density (no vapour-rich FI), with low to intermediate salinity (<11.5 wt.% eq. NaCl) and are reduced as suggested by the presence of CO_2 and CH_4. Fluid trapping temperature calculations could not be carried out from the microthermometric study. However, we assume that gold precipitated from high to medium T fluids (450 to 350-250°C), with fS_2 ranging from 10^{-7} to 10^{-11} atm taking into account the arsenopyrite geothermometry and up to 10^{-14} atm considering the lowest Th. Moreover, the loellingite, arsenopyrite and pyrrhotite mineral assemblage and high content of FeS (*ca.*, 10 mol%) in sphalerite reinforce a low sulfidation state that prevailed during the formation of the deposit (Einaudi et al., 2003). This suggests that fluids are related to a medium to S-poor environment. Hydrothermal fluids of metamorphic and magmatic origins are therefore reduced as herein suggested by the CH_4 occurrences in FIA. So, they must be enriched in highly reactive hydrogen sulphide complexes, which are common species at such temperatures (Kouzmanov and Pokrovsky, 2012). Chloride complexes are also involved in the mineralizing processes because they more effectively transport base metals (Cu and Ag). According to Kouzmanov and Pokrovsky (2012), precipitation of base metal sulphides probably occurs in response to decreasing temperature (i.e., their solubility decreases two orders of magnitude between 350 and 250°C). As muscovite crystallization leads to pH increase, it may also affect base metal sulphide precipitation (i.e., their solubility decreases two orders of magnitude between pH 3 and 5). Our results also show that, during cooling, mineralizing fluids become enriched in CO_2 while CH_4 content decreases. In such cases, the transport of gold is in the form of $Au(HS)^{2-}$ in S-rich environments, but decreases significantly with increasing CO_2 concentration (Kokh et al., 2017). Thus in S-poor environments, the solubility may be assumed by the neutral complex, $Au(HS)^0$, which is practically unaffected by the presence of CO_2, unlike $Au(HS)^{2-}$.

In such a context, two main processes may govern the precipitation of gold and pyrite: pressure drops and sulfidization of some Fe-bearing phase in the hornfels. Cyclic fluid-activated seismic valves may cause drops in pressure during hydrofracturing causing a large decrease in gold solubility and also increasing

pH, which destabilizes gold-rich hydrogen sulphide complexes (Loucks and Mavrogenes, 1999). Sulfidization of the hornfels is shown by the following reaction:

$$2Au(HS)^0 + FeO \Leftrightarrow FeS_2 + 2Au + H_2O \quad (7),$$

where FeO represents reactive iron from country rocks (*i.e.*, iron oxides, biotite). According to Pokrovski et al. (2002), ongoing sulfidization process may explain the formation of arsenopyrite by replacement of pyrite from reaction (7) as follow:

$$As(OH)_3^0 + FeS_2 + \Leftrightarrow FeAsS + H_2S + 1.25O_2 + 0.5H_2O \quad (8).$$

This thus explains replacement of disseminated iron oxides by sulfides within country rocks and the probable alteration of metamorphic biotite, andalusite and cordierite into chlorite and sericite. The source of metal remains uncertain and may derive from late granodioritic fluid exsolution, melted country rocks, or leaching of country rocks and/or granodiorite.

These observations are consistent with numerous fluids of this type (*i.e.*, H_2O- N_2-CH_4-(CO_2)) that result from graphite-fluid equilibrium and which have been reported in graphitic hornfels (Bebout et al., 1999; Cathelineau et al., 1990; Wilkinson, 1991) and intrusion-related Sn–W-Au provinces (Mair et al., 2006).

5.3. *Regional implications*

In this study, we propose a tectono-magmatic model for the evolution of the Boumalne inlier in three main stages involving the emplacement of an intrusion-related gold deposit (Fig. 18). **i**) The first stage refers to the top-to-the-south asymmetry and the syn-kinematic Ikniwn pluton emplacement at *ca.*, 563 Ma (Fig. 18a). Concerning the southward vergence, such features remain enigmatic because these motions cannot be attributed to some gravitational effects coeval with the granodiorite emplacement. Even if a roughly N-S trending earlier compressional event has been already suggested to affect this part of the Jbel Saghro (Saquaque et al., 1992), we cannot be sure that this stage developed at a regional scale (*i.e.*, N-S trending regional direction of shortening) or if it remained local and was developed under deviatoric stress within a transpressive regime (*i.e.*, local deviation of the ESE-WNW shortening direction). Indeed, in this latter case, description of large-scale "en-echelon" overturned folds, thrusts in the Boumalne and the comparable Imiter basin inliers and even coeval N090°E to N070°E strike-slip faults would suggest the existence of a transpressional regime under an approximately NW-SE shortening direction, as already proposed by Ighid et al. (1989) and Tuduri (2005). Concerning the related synkinematic pluton, such an assumption can be reasonably attributed to the emplacement of the voluminous Ikniwn granodiorite as metamorphic spots highlight the N-S lineation and define the top-to-the-south asymmetry. Similar observations were also made by Ighid et al. (1989) in the Imiter basin inlier where the Taouzzakt and Bou Teglimt granodiorite intrusions have been considered as syn-kinematic. Age of the Ikniwn granodiorite intrusion is herein proposed at 563.5 ± 6.3 Ma, which is in good agreement with the ages of some plutons in the Imiter inlier: the Taouzzakt granodiorite (572 ± 5 Ma; Cheilletz et al., 2002), the Bou Teglimt granodiorite (567 ± 6 Ma; Baidada et al., 2001) and the Igoudrane diorite (565 ± 5 Ma; De Wall et al., 2001). **ii**) The second stage is linked to a magmatic-hydrothermal

transition and ore deposition. It developed migmatization highlighted by *in situ* leucocratic structures, then aplitic and pegmatitic injections, besides intermediate and striped quartz veins during a large-scale ENE-WSW dextral shearing process that results from an ESE-WNW shortening direction during transtensive tectonics (Fig. 18b). Such magmatic features are developed in response to partial melting of metasedimentary country rocks in response to, at a minimum, heat transfer from the underlying Ikniwn intrusion. The main Au-mineralization was concentrated during this event. The regular and parallel vein array results from the re-using of pre-existing N070°E cleavage planes (Figs. 16 and 17). In this model, we suggest that the W-Au Taourirt-Tamellalt prospect belongs to the same stage and thus was formed by similar processes. The emplacement age of this magmatic-hydrothermal system must have been synchronous or slightly later with respect to the Ikniwn intrusion, but it must remain connected to its high thermal influx. Direct *in situ* dating of mineralization has been performed on apatite by the LA-ICP-MS U-Pb method, but was unsuccessful because of their low U and high common Pb contents. In any case, we consider that this vein system was emplaced between the 570 to 558 Ma interval (Ikniwn intrusion) but before the 559 to 551 Ma interval (Isk n'Alla granite). Several attempts to date the Taourirt-Tamellalt were made providing the following results: 550 ± 33 Ma (whole-rock Rb-Sr; Mrini, 1993) and 645 ± 12 Ma (U-Pb zircon; Massironi et al., 2007). If we may discard the Rb-Sr method considering the large error, the U-Pb zircon could represent an emplacement age. However, we herein suggest following our observations that such an age is probably due to the presence of inherited zircon grains that would be abundant in any leucosome.

Eventually, the transition between the transpressional stage 1 and the transtensional stage 2 regimes occurred, while the shortening direction (parallel to Z strain axis) remained roughly constant (*i.e.*, NW-SE to WNW-ESE). However, one can note a shift in the two other strain directions showing a decreasing in the vertical extension that becomes horizontal. In such a model, the Ikniwn granodiorite (more precisely the contact aureole) records the transition between transpressional and transtensional regimes. This is consistent with the assumption made by Walsh et al. (2012), which suggested that the transition from transpression to transtension occured at *ca.* 560 Ma.

iii) The final stage is primarily associated with ~ N-S wrench faulting that affects previous features, volcanic dyke emplacement along the N070°E trending direction, followed then by the pink granite emplacement (Fig. 18c). Although we suggest this event occurred between 560 and 540 Ma, little data is available concerning its structural control. One can possibly suggest a N-S trending extension with respect to dyke emplacement. Strike-slip faults would correspond to transfer faults.

6. Conclusions

The present study demonstrates that the Thaghassa deposit, which occurs within hornfelsed graphitic metasediments, is relevant to the origin of an intrusion-related gold setting. It proposes a new contribution, based on mineralogical and structural data with various microthermometry and U-Pb geochronology studies that are in agreement with the existence of a genetic link between magmatic and

hydrothermal processes in IRG deposits. However, the Thaghassa area displays an atypical association beginning during migmatization processes then evolved from magmatic, magmatic-hydrothermal to hydrothermal features that are not commonly described in other mineralized vein systems. We thus propose a progressive and continuous vein formation model that began during the migmatization stage, developed an intermediate vein system and was completed within hydrothermal conditions. Fluid inclusions study and mineral geothermometry suggests that the system evolved from hot fluids (~550°C) dominated by N_2 and CH_4 to intermediate temperature (~300 to 450°C) aquo-carbonic fluids in the system (H_2O-NaCl-CO_2) + CH_4. Gold precipitation is related to intermediate temperature mineralizing fluids that have strongly interacted with the hornfelsed country rocks. The formation of veins of intermediate composition (magmatic-hydrothermal system) thus indicates the persistence of a magmatic character, at least until the beginning of the hydrothermal process. All these events follow a compressional or transpressional stage and occurred within both a similar tectonic setting (transtensional) and structural environment. The progressive deformation reactivates the previously formed structures. We emphasize in this study the significant improvement that represents the combined study of mineralogical, textural and structural data in the study of polyphase vein system formation. At last, we highlight that in hornfels-hosted IRG deposits, fluid sources may both originate from magmatic processes and devolatilization of the metamorphic host rocks. Future research should continue building a focus on the source of metals.

Acknowledgements

This work has been undertaken with the help of the French-Moroccan programs “Action Intégrée n° 222/STU/00”. REMINEX exploration team and SMI mining company provided funds and logistics for field and laboratory studies. We particularly acknowledge El Hajj Bouiroukouten and the intern geologists of MANAGEM for their constant help and support. We are grateful to Olivier Rouer and Gilles Drouet for assistance and help with electronic microprobe analyses. Authors thank Thibaut Chamel for zircon dating preparations, Yannick Branquet for attempting apatite dating, and Daniel Gerger for the editing. Stanislas Sizaret and Kalin Kouzmanov provided many suggestions concerning metal speciation and fluid interactions with rocks and minerals. We also gratefully thank Prof. Franco Pirajno and Prof. Ilkay Kuscu for the editorial comments, and Prof. David Lentz and Dr. Nilay Gülyüz, who provided valuable advice that substantially improved the manuscript.

References

Al Ansari, A.E., Sagon, J.P., 1997. Le gisement d'or de Tiouit (Jbel Saghro, Anti-Atlas, maroc). Un système mésothermal polyphasé à sulfures-or et hématite-or dans une granodiorite potassique d'âge Protérozoïque supérieur. Chronique de la Recherche Minière 527, 3-25.

Ardia, P., Hirschmann, M.M., Withers, A.C., Stanley, B.D., 2013. Solubility of CH_4 in a synthetic basaltic melt, with applications to atmosphere–magma ocean–core partitioning of volatiles and to the evolution of the Martian atmosphere. Geochimica et Cosmochimica Acta 114, 52-71.

Baidada, B., Ikenne, M., Barbey, P., Alansari, A., Soulaimani, A., Cousens, B., Faouziya, H., Ilmen, S., 2017. New zircon U-Pb ages of the Imiter granitoids (Saghro massif, eastern Anti-Atlas, Morocco): Geodynamic implications, in: Mouttaqi, A., Saddiqi, O. (Eds.), The First West African Craton and Margins International Workshop: WACMA1, Dakhla, Morocco p. 44.

Baker, T., Lang, J., 2001. Fluid inclusion characteristics of intrusion-related gold mineralization, Tombstone–Tungsten magmatic belt, Yukon Territory, Canada. Mineralium Deposita 36, 563-582.

Ballouard, C., Boulvais, P., Poujol, M., Gapais, D., Yamato, P., Tartèse, R., Cuney, M., 2015. Tectonic record, magmatic history and hydrothermal alteration in the Hercynian Guérande leucogranite, Armorican Massif, France. Lithos 220–223, 1-22.

Barbey, P., Oberli, F., Burg, J.P., Nachit, H., Pons, J., Meier, M., 2004. The Palaeoproterozoic in western Anti-Atlas (Morocco): a clarification. Journal of African Earth Sciences 39, 239-245.

Barton, P.B., Toulmin, P., 1966. Phase relations involving sphalerite in the Fe-Zn-S system. Economic Geology 61, 815-849.

Bebout, G.E., Cooper, D.C., Bradley, A.D., Sadofsky, S.J., 1999. Nitrogen-isotope record of fluid-rock interactions in the Skiddaw aureole and granite, English Lake District. American Mineralogist 84, 1495-1505.

Benkirane, Y., 1987. Les minéralisations à W (Sn, Mo, Au, Bi, Ag, Cu, Pb, Zn) du granite de Taourirt-Tamellalt dans leur cadre géologique, la boutonnière protérozoïque du SE de Boumalne du Dadès (Saghro oriental, Anti-Atlas, Maroc). Université de Paris VI, France, p. 375.

Benziane, F., 2007. Lithostratigraphie et évolution géodynamique de l'anti-Atlas (Maroc) du paléoprotérozoïque au néoprotérozoïque: exemples de la boutonnière de Tagragra Tata et du Jebel Saghro. Université de Chambéry, Chambéry, France, p. 320.

Beyssac, O., Goffé, B., Chopin, C., Rouzaud, J.N., 2002. Raman spectra of carbonaceous material in metasediments: a new geothermometer. Journal of Metamorphic Geology 20, 859-871.

Bierlein, F.P., McKnight, S., 2005. Possible intrusion-related gold systems in the western Lachlan Orogen, southeast Australia. Economic Geology 100, 385-398.

Blein, O., Baudin, T., Chèvremont, P., Soulaimani, A., Admou, H., Gasquet, P., Cocherie, A., Egal, E., Youbi, N., Razin, P., Bouabdelli, M., Gombert, P., 2014. Geochronological constraints on the polycyclic magmatism in the Bou Azzer-El Graara inlier (Central Anti-Atlas Morocco). Journal of African Earth Sciences 99, Part 2, 287-306.

Bodnar, R.J., 1993. Revised equation and table for determining the freezing point depression of H_2O-Nacl solutions. Geochimica et Cosmochimica Acta 57, 683-684.

Boiron, M.-C., Cathelineau, M., Banks, D.A., Fourcade, S., Vallance, J., 2003. Mixing of metamorphic and surficial fluids during the uplift of the Hercynian upper crust: consequences for gold deposition. Chemical Geology 194, 119-141.

Bons, P.D., Elburg, M.A., Gomez-Rivas, E., 2012. A review of the formation of tectonic veins and their microstructures. Journal of Structural Geology 43, 33-62.

Bouabdellah, M., Maacha, L., Jébrak, M., Zouhair, M., 2016. Re/Os Age Determination, Lead and Sulphur Isotope Constraints on the Origin of the Bouskour Cu–Pb–Zn Vein-Type Deposit (Eastern Anti-Atlas, Morocco) and Its

Relationship to Neoproterozoic Granitic Magmatism, in: Bouabdellah, M., Slack, J.F. (Eds.), Mineral Deposits of North Africa. Springer International Publishing, Cham, pp. 277-290.

Burke, E.A.J., 2001. Raman microspectrometry of fluid inclusions. Lithos 55, 139-158.

Burkhard, M., Caritg, S., Helg, U., Robert-Charrue, C., Soulaimani, A., 2006. Tectonics of the Anti-Atlas of Morocco. Comptes Rendus Geoscience 338, 11-24.

Cathelineau, M., Lespinasse, M., Bastoul, A.M., Bernard, C., Leroy, J., 1990. Fluid Migration During Contact Metamorphism: The Use of Oriented Fluid Inclusion Trails for a Time/Space Reconstruction. Mineralogical Magazine 54, 375.

Cepedal, A., Fuertes-Fuente, M., Martín-Izard, A., García-Nieto, J., Boiron, M.C., 2013. An intrusion-related gold deposit (IRGD) in the NW of Spain, the Linares deposit: Igneous rocks, veins and related alterations, ore features and fluids involved. Journal of Geochemical Exploration 124, 101-126.

Chaker, M., 1997. Géochimie et métallogénie de la mine d'or de Tiouit, Anti-Atlas oriental, Sud du Maroc. Université du Québec à chicoutimi (UQAC), Chicoutimi, Québec, Canada, p. 325.

Chauvet, A., Volland-Tuduri, N., Lerouge, C., Bouchot, V., Monié, P., Charonnat, X., Faure, M., 2012. Geochronological and geochemical characterization of magmatic-hydrothermal events within the Southern Variscan external domain (Cévennes area, France). International Journal of Earth Sciences 101, 69-86.

Cheilletz, A., Levresse, G., Gasquet, D., Azizi-Samir, M.R., Zyadi, R., Archibald, A.D., Farrar, E., 2002. The giant Imiter silver deposit: Neoproterozoic epithermal mineralization in the Anti-Atlas, Morocco. Mineralium Deposita 37, 772-781.

Choubert, G., 1963. Histoire géologique du Précambrien de l'Anti-Atlas de l'Archéen à l'aurore des temps primaires. Notes et Mémoires du Service Géologique du Maroc 162, 352.

Cox, S.F., 1987. Antitaxial crack-seal vein microstructures and their relationship to displacement paths. Journal of Structural Geology 9, 779-787.

Cox, S.F., Etheridge, M.A., 1983. Crack-seal fiber growth mechanisms and their significance in the development of oriented layer silicate microstructures. Tectonophysics 92, 147-170.

De Wall, H., Kober, B., Errami, E., Ennih, N., Greiling, R.O., 2001. Age de mise en place et contexte géologique des granitoïdes de la boutonnière d'Imiter (Saghro oriental, Anti-Atlas, Maroc), 2ème Colloque International 3MA (Magmatisme, Métamorphisme & Minéralisations Associées), Marrakech (Maroc), p. 19.

Delchini, S., Lahfid, A., Plunder, A., Michard, A., 2016. Applicability of the RSCM geothermometry approach in a complex tectono-metamorphic context: The Jebilet massif case study (Variscan Belt, Morocco). Lithos 256–257, 1-12.

Dubessy, J., Poty, B., Ramboz, C., 1989. Advances in C-O-H-N-S fluid geochemistry based on micro-Raman spectrometric analysis of fluid inclusions. European Journal of Mineralogy 1, 517-534.

Einaudi, M.T., Hedenquist, J.W., Inan, E.E., 2003. Sulfidation state of fluids in active and extinct hydrothermal systems: transitions from porphyry to epithermal environments, in: Simmons, S.F., Graham, I. (Eds.), Volcanic, geothermal, and ore-forming fluids: rulers and witnesses of processes within the Earth. Society of Economic Geologists, pp. 285-313.

El Hadi, H., Simancas, J.F., Martínez-Poyatos, D., Azor, A., Tahiri, A., Montero, P., Fanning, C.M., Bea, F., González-Lodeiro, F., 2010. Structural and geochronological constraints on the evolution of the Bou Azzer Neoproterozoic ophiolite (Anti-Atlas, Morocco). Precambrian Research 182, 1-14.

Eldursi, K., Branquet, Y., Guillou-Frottier, L., Marcoux, E., 2009. Numerical investigation of transient hydrothermal processes around intrusions: Heat-transfer and fluid-circulation controlled mineralization patterns. Earth and Planetary Science Letters 288, 70-83.

Errami, E., Olivier, P., 2012. The Iknioun granodiorite, tectonic marker of Ediacaran SE-directed tangential movements in the Eastern Anti-Atlas, Morocco. Journal of African Earth Sciences 69, 1-12.

Essarraj, S., Boiron, M.C., Cathelineau, M., Fourcade, S., 2001. Multistage deformation of Au-quartz veins (Laurieras, French Massif Central): evidence for a late gold introduction from microstructural, isotopic and fluid inclusion studies. Tectonophysics 336, 79-99.

Essarraj, S., Boiron, M.-C., Cathelineau, M., Tarantola, A., Leisen, M., Boulvais, P., Maacha, L., 2016. Basinal Brines at the Origin of the Imiter Ag-Hg Deposit (Anti-Atlas, Morocco): Evidence from LA-ICP-MS Data on Fluid Inclusions, Halogen Signatures, and Stable Isotopes (H, C, O). Economic Geology 111, 1753-1781.

Fekkak, A., Pouclet, A., Badra, L., 2002. The Pre-Panafrican rifting of Saghro (Anti-Atlas, Morocco) : exemple of the middle Neoproterozoic Basin of Boumalne. Bulletin de la Société Géologique de France 173, 25-35.

Fekkak, A., Pouclet, A., Ouguir, H., Ouazzani, H., Badra, L., Gasquet, D., 2001. Géochimie et signification géotectonique des volcanites du Cryogénien inférieur du Saghro (Anti-Atlas oriental, Maroc). Geodinamica Acta 13, 1-13.

Finger, F., Clemens, J.D., 1995. Migmatization and "secondary" granitic magmas: effects of emplacement and crystallization of "primary" granitoids in Southern Bohemia, Austria. Contributions to Mineralogy and Petrology 120, 311-326.

Fontboté, L., Kouzmanov, K., Chiaradia, M., Pokrovski, G.S., 2017. Sulfide minerals in hydrothermal deposits. Elements 13, 97-103.

Fournier, R.O., 1999. Hydrothermal processes related to movement of fluid from plastic into brittle rock in the magmatic-epithermal environment. Economic Geology 94(8): 1193-1211.

Gasquet, D., Levresse, G., Cheilletz, A., Azizi-Samir, M.R., Mouttaqi, A., 2005. Contribution to a geodynamic reconstruction of the Anti-Atlas (Morocco) during Pan-African times with the emphasis on inversion tectonics and metallogenic activity at the Precambrian-Cambrian transition. Precambrian Research 140, 157-182.

Genier, F., Bussy, F., Epard, J.-L., Baumgartner, L., 2008. Water-assisted migmatization of metagraywackes in a Variscan shear zone, Aiguilles-Rouges massif, western Alps. Lithos 102, 575-597.

Gloaguen, E., Branquet, Y., Chauvet, A., Bouchot, V., Barbanson, L., Vigneresse, J.-L., 2014. Tracing the magmatic/hydrothermal transition in regional low-strain zones: The role of magma dynamics in strain localization at pluton roof, implications for intrusion-related gold deposits. Journal of Structural Geology 58, 108-121.

Goldstein, R.H., Reynolds, T.J., 1994. Systematics of fluid inclusions in diagenetic minerals, in: Goldstein, R.H., Reynolds, T.J. (Eds.), SEPM short course. Society for Sedimentary Geology, p. 199.

Gouiza, M., Charton, R., Bertotti, G., Andriessen, P., Storms, J.E.A., 2017. Post-Variscan evolution of the Anti-Atlas belt of Morocco constrained from low-temperature geochronology. International Journal of Earth Sciences 106, 593-616.

Guidotti, C.V., 1984. Micas in metamorphic rocks, in: Bailey, S.W. (Ed.), Micas. Mineralogical Society of America, Washington, pp. 357-467.

Halter, W.E., Webster, J.D., 2004. The magmatic to hydrothermal transition and its bearing on ore-forming systems - Preface. Chemical Geology 210, 1-6.

Hart, C.J., 2007. Reduced intrusion-related gold systems. Mineral Deposits of Canada: A synthesis of Major deposit types, district metallogeny, the Evolution of geological provinces, and exploration methods: Geological Association of Canada, Mineral Deposits Division, Special Publication, 95-112.

Hart, C.J.R., Mair, J.L., Goldfarb, R.J., Groves, D.I., 2004. Source and redox controls on metallogenic variations in intrusion-related ore systems, Tombstone-Tungsten Belt, Yukon Territory, Canada. Geological Society of America Special Papers 389, 339-356.

Hawkins, M.P., Beddoe-Stephens, B., Gillespie, M.R., Loughlin, S., Barron, H.F., Barnes, R.P., Powell, J.H., Waters, C.N., Williams, M., 2001a. Carte géologique du Maroc au 1/50 000, feuille Tiwit. Notes et Mémoires du Service Géologique du Maroc 404.

Hawkins, M.P., Beddoe-Stephens, B., Gillespie, M.R., Loughlin, S., Barron, H.F., Barnes, R.P., Powell, J.H., Waters, C.N., Williams, M., 2001b. Carte géologique du Maroc au1/50 000, feuille Ikniwn. Notes et Mémoires du Service Géologique du Maroc 405.

Hefferan, K., Soulaimani, A., Samson, S.D., Admou, H., Inglis, J., Saquaque, A., Latifa, C., Heywood, N., 2014. A reconsideration of Pan African orogenic cycle in the Anti-Atlas Mountains, Morocco. Journal of African Earth Sciences 98, 34-46.

Hilgers, C., Koehn, D., Bons, P.D., Urai, J.L., 2001. Development of crystal morphology during unitaxial growth in a progressively widening vein : II. Numerical simulations of the evolution of antitaxial fibrous veins. Journal of Structural Geology 23, 873-885.

Hindermeyer, J., 1953. Le Précambrien I et le Précambrien II du Saghro. Comptes rendus hebdomadaires des séances de l'Académie des sciences 237, 921-923.

Hindermeyer, J., Choubert, G., Destombes, J., Gauthier, H., 1977. Carte géologique de l'Anti-Atlas oriental : feuille Dadès et Jbel Saghro 1/200 000., Notes et Mémoires du Service Géologique du Maroc.

Hollard, H., Choubert, G., Bronner, G., Marchand, J., Sougy, J., 1985. Carte géologique du Maroc, échelle: 1/1.000.000. . Notes et Mémoires du Service Géologique du Maroc 260.

Holtz, F., Johannes, W., 1994. Maximum and minimum water contents of granitic melts: implications for chemical and physical properties of ascending magmas. Lithos 32, 149-159.

Hulin, C., Dubois, M., Tuduri, J., Chauvet, A., Boulvais, P., Gaouzi, A., Mouhajir, M., Essalhi, M., Outhounjite, S., 2013. New fluid inclusions and oxygen isotope data to constrain a formation model for the Imiter Ag world class deposit (Anti-Atlas, Morocco), ECROFI XXII, Antalya, Turkey, pp. 78-79.

Icenhower, J., London, D., 1995. An experimental study of element partitioning among biotite, muscovite, and coexisting peraluminous silicic melt at 200 MPa (H_2O), American Mineralogist, p. 1229.

Ighid, L., Saquaque, A., Reuber, I., 1989. Plutons syn-cinématiques et la déformation panafricaine majeure dans le Saghro oriental (boutonnière d'Imiter, Anti-Atlas, Maroc). Comptes Rendus de l'Académie des Sciences, Série II Mécanique-physique, Chimie, Sciences de l'univers, Sciences de la Terre 309, 615-620.

Ikenne, M., Söderlund, U., Ernst, R.E., Pin, C., Youbi, N., El Aouli, E.H., Hafid, A., 2017. A c. 1710 Ma mafic sill emplaced into a quartzite and calcareous series from Ighrem, Anti-Atlas – Morocco: Evidence that the Taghdout passive margin sedimentary group is nearly 1 Ga older than previously thought. Journal of African Earth Sciences 127, 62-76.

Inglis, J.D., D'Lemos, R.S., Samson, S.D., Admou, H., 2005. Geochronological constraints on late Precambrian intrusions, metamorphism, and tectonism in the Anti-Atlas mountains. The Journal of Geology 113, 439-450.

Jackson, S.E., Pearson, N.J., Griffin, W.L., Belousova, E.A., 2004. The application of laser ablation-inductively coupled plasma-mass spectrometry to *in situ* U–Pb zircon geochronology. Chemical Geology 211, 47-69.

Jakobsson, S., Holloway, J.R., 1986. Crystal — Liquid experiments in the presence of a C-O-H fluid buffered by graphite + iron + wustite: Experimental method and near-liquidus relations in basanite. Journal of Volcanology and Geothermal Research 29, 265-291.

Jensen, E.P., Barton, M.D., 2000. Review in Economic Geology. Gold deposits related to alkaline magmatism, in: Hagemann, S.G., Brown, P.E. (Eds.), Gold in 2000. Society of Economic Geology, Inc, Boulder, pp. 279-314.

Johannes, W., 1983. On the origin of layered migmatites, in: Atherton, M.P., Gribble, C.D. (Eds.), Migmatites, melting and metamorphism. Shiva, Nantwich, United Kingdom, pp. 234-248.

Koehn, D., Passchier, C.W., 2000. Shear sense indicators in striped bedding-veins. Journal of Structural Geology 22, 1141-1151.

Kokh, M.A., Akinfiev, N.N., Pokrovski, G.S., Salvi, S., Guillaume, D., 2017. The role of carbon dioxide in the transport and fractionation of metals by geological fluids. Geochimica et Cosmochimica Acta 197, 433-466.

Kontak, D., Kyser, K., 2011. A fluid inclusion and isotopic study of an intrusion-related gold deposit (IRGD) setting in the 380 Ma South Mountain Batholith, Nova Scotia, Canada: evidence for multiple fluid reservoirs. Mineralium Deposita 46, 337-363.

Kouzmanov, K., Pokrovski, G.S., 2012. Hydrothermal controls on metal distribution in porphyry Cu (-Mo-Au) systems, in: Hedenquist, J.W., Harris, M., Camus, F. (Eds.), Geology and genesis of major copper deposits and districts of the world: a tribute to Richard H. Sillitoe. Special Publications of the Society of Economic Geologists, pp. 573-618.

Kretschmar, U., Scott, S.D., 1976. Phase relations involving arsenopyrite in the system Fe-As-S and their application. The Canadian Mineralogist 14, 364-386.

Lahfid, A., Beyssac, O., Deville, E., Negro, F., Chopin, C., Goffé, B., 2010. Evolution of the Raman spectrum of carbonaceous material in low-grade metasediments of the Glarus Alps (Switzerland). Terra Nova 22, 354-360.

Lang, J.R., Baker, T., 2001. Intrusion-related gold systems: the present level of understanding. Mineralium Deposita 36, 477-489.

Leblanc, M., Lancelot, J.R., 1980. Interprétation géodynamique du domaine panafricain (Précambrien terminal) de l'Anti-Atlas (Maroc) à partir de données géologiques et géochronologiques. Canadian Journal of Earth Sciences 17, 142-155.

Libourel, G., Marty, B., Humbert, F., 2003. Nitrogen solubility in basaltic melt. Part I. Effect of oxygen fugacity. Geochimica et Cosmochimica Acta 67, 4123-4135.

Loucks, R.R., Mavrogenes, J.A., 1999. Gold Solubility in Supercritical Hydrothermal Brines Measured in Synthetic Fluid Inclusions. Science 284, 2159-2163.

Lowenstern, J.B., 2001. Carbon dioxide in magmas and implications for hydrothermal systems. Mineralium Deposita 36, 490-502.

Ludwig, K.R., 2001. Isoplot/Ex Version 2.49. A geochronological toolkit for Microsoft Excel. Berkeley Geochronology Center.

Mair, J.L., Farmer, G.L., Groves, D.I., Hart, C.J.R., Goldfarb, R.J., 2011. Petrogenesis of postcollisional magmatism at Scheelite Dome, Yukon, Canada: evidence for a lithospheric mantle Ssource for magmas associated with intrusion-related gold systems. Economic Geology 106, 451-480.

Mair, J.L., Goldfarb, R.J., Johnson, C.A., Hart, C.J.R., Marsh, E.E., 2006. Geochemical constraints on the genesis of the Scheelite Dome intrusion-related gold deposit, Tombstone Gold Belt, Yukon, Canada. Economic Geology 101, 523-553.

Marcoux, É., Nerci, K., Branquet, Y., Ramboz, C., Ruffet, G., Peucat, J.-J., Stevenson, R., Jébrak, M., 2015. Late-Hercynian intrusion-related gold deposits: An integrated model on the Tighza polymetallic district, central Morocco. Journal of African Earth Sciences 107, 65-88.

Massironi, M., Moratti, G., Algouti, A., Benvenuti, M., Dal Piaz, G.V., Eddebi, A., El Boukhari, A., Laftouhi, N., Ounaimi, H., Schiavo, A., Taj Eddine, K., Visonà, D., 2007. Carte géologique du Maroc au 1/50000, feuille Boumalne. Notes et Mémoires du Service Géologique du Maroc 521.

McLellan, E.L., 1983. Contrasting textures in metamorphic and anatectic migmatites: an example from the Scottish Caledonides. Journal of Metamorphic Geology 1, 241-262.

Milési, J.-P., Feybesse, J.-L., Pinna, P., Deschamps, Y., Kampunzu, H.A.B., Muhongo, S., Lescuyer, J.L., Toteu, S.F., 2004. Geology and major ore deposits of Africa, 20th Colloquium of African Geology ed. BRGM, Orléans-France.

Missenard, Y., Zeyen, H., Frizon de Lamotte, D., Leturmy, P., Petit, C., Sébrier, M., Saddiqi, O., 2006. Crustal versus asthenospheric origin of relief of the Atlas Mountains of Morocco. Journal of Geophysical Research, Solid Earth 111, B03401.

Monier, G., Robert, J.L., 1986. Muscovite solid solutions in the system K_2O, MgO, FeO, AL_2O_3, SiO_2, H_2O : an experimental study at 2 kbar PH2O and comparison with natural Li-free white micas. Mineralogical Magazine 50, 257-266.

Mrini, Z., 1993. Chronologie (Rb-Sr ; U-Pb) ; traçage isotopique (Sr-Nd-Pb) des sources des roches magmatiques éburnéennes, panafricaines et hercyniennes du Maroc. Université Cadi Ayyad, Marrakech, Maroc, p. 227.

Mustard, R., 2001. Granite-hosted gold mineralization at Timbarra, Northern New South Wales, Australia. Mineralium Deposita 36, 542-562.

Mustard, R., Ulrich, T., Kamenetsky, V.S., Mernagh, T., 2006. Gold and metal enrichment in natural granitic melts during fractional crystallization. Geology 34, 85-88.

O'Connor, E., Barnes, R., Beddoe-Stephens, B., Fletcher, T., Gillespie, M., Hawkins, M., Loughlin, S., Smith, M., Smith, R., Waters, C., 2010. Geology of the Drâa, Kerdous, and Boumalne districts, Anti-Atlas, Morocco. British Geological Survey, Keyworth, Nottingham, p. 310.

Oliver, N., Barr, T., 1997. The geometry and evolution of magma pathways through migmatites of the Halls Creek Orogen, Western Australia. Mineralogical Magazine 61, 3-14.

Ouguir, H., Macaudière, J., Dagallier, G., 1996. Le Protérozoïque supérieur d'Imiter, Saghro oriental, Maroc : un contexte géodynamique d'arrière arc. Journal of African Earth Sciences 22, 173-189.

Passchier, C.W., Simpson, C., 1986. Porphyroclast systems as kinematic indicators. Journal of Structural Geology 8, 831-843.

Pattison, D.R.M., DeBuhr, C.L., 2015. Petrology of metapelites in the Bugaboo aureole, British Columbia, Canada. Journal of Metamorphic Geology 33, 437-462.

Pattison, D.R.M., Harte, B., 1988. Evolution of structurally contrasting anatectic migmatites in the 3-kbar Ballachulish aureole, Scotland. Journal of Metamorphic Geology 6, 475-494.

Pokrovski, G.S., Kara, S., Roux, J., 2002. Stability and solubility of arsenopyrite, FeAsS, in crustal fluids. Geochimica et Cosmochimica Acta 66, 2361-2378.

Pupin, J.P., 1980. Zircon and granite petrology. Contributions to Mineralogy and Petrology 73, 207-220.

Ridolfi, F., Renzulli, A., Puerini, M., 2010. Stability and chemical equilibrium of amphibole in calc-alkaline magmas: an overview, new thermobarometric formulations and application to subduction-related volcanoes. Contributions to Mineralogy and Petrology 160, 45-66.

Rowins, S.M., Groves, D.I., McNaughton, N.J., Palmer, M.R., Eldridge, C.S., 1997. A reinterpretation of the role of granitoids in the genesis of Neoproterozoic gold mineralization in the Telfer Dome, Western Australia. Economic Geology 92, 133-160.

Saquaque, A., Benharref, M., Abia, H., Mrini, Z., Reuber, I., Karson, J.A., 1992. Evidence for a Panafrican volcanic arc and wrench fault tectonics in Jbel Saghro, Morocco. Geologische Rundschau 81, 1-13.

Sawyer, E.W., 2008. Atlas of Migmatites, in: Cavers, P.B. (Ed.), The Canadian Mineralogist. NRC Research Press, Ottawa, Ontario, Canada, p. 371.

Schiavo, A., Taj Eddine, K., Algouti, A., Benvenuti, M., Dal Piaz, G.V., Eddebi, A., El Boukhari, A., Laftouhi, N., Massironi, M., Ounaimi, H., Pasquarè, G., Visonà, D., 2007. Carte géologique du Maroc au 1/50000, feuille Imtir. Notes et Mémoires du Service Géologique du Maroc 518.

Schmidt, M.W., 1992. Amphibole composition in tonalite as a function of pressure: an experimental calibration of the Al-in-hornblende barometer. Contributions to Mineralogy and Petrology 110, 304-310.

Sharp, Z.D., Essene, E.J., Kelly, W.C., 1985. A re-examination of the arsenopyrite geothermometer; pressure considerations and applications to natural assemblages. The Canadian Mineralogist 23, 517-534.

Sibson, R.H., Robert, F., Poulsen, K.H., 1988. High-angle reverse faults, fluid-pressure cycling, and mesothermal gold-quartz deposits. Geology 16, 551-555.

Sláma, J., Košler, J., Condon, D.J., Crowley, J.L., Gerdes, A., Hanchar, J.M., Horstwood, M.S.A., Morris, G.A., Nasdala, L., Norberg, N., Schaltegger, U., Schoene, B., Tubrett, M.N., Whitehouse, M.J., 2008. Plešovice zircon - A new natural reference material for U–Pb and Hf isotopic microanalysis. Chemical Geology 249, 1-35.

Symmes, G.H., Ferry, J.M., 1995. Metamorphism, Fluid Flow and Partial Melting in Pelitic Rocks from the Onawa Contact Aureole, Central Maine, USA. Journal of Petrology 36, 587-612.

Thomas, R.J., Chevallier, L.P., Gresse, P.G., Harmer, R.E., Eglington, B.M., Armstrong, R.A., de Beer, C.H., Martini, J.E.J., de Kock, G.S., Macey, P.H., Ingram, B.A., 2002. Precambrian evolution of the Sirwa Window, Anti-Atlas Orogen, Morocco. Precambrian Research 118, 1-57.

Thomas, R.J., Fekkak, A., Ennih, N., Errami, E., Loughlin, S.C., Gresse, P.G., Chevallier, L.P., Liegeois, J.-P., 2004. A new lithostratigraphic framework for the Anti-Atlas Orogen, Morocco. Journal of African Earth Sciences 39, 217-226.

Thompson, J.F.H., Newberry, R.J., 2000. Gold deposits related to reduced granitic intrusions, in: Hagemann, S.G., Brown, P.E. (Eds.), Review in Economic Geology: Gold in 2000. Society of Economic Geology, Inc, Boulder, pp. 377-400.

Thompson, J.F.H., Sillitoe, R.H., Baker, T., Lang, J.R., Mortensen, J.K., 1999. Intrusion-related gold deposits associated with tungsten-tin provinces. Mineralium Deposita 34, 323-334.

Thorne K.G., Lentz D.R., Hoy D., Fyffe L.R., Cabri L.J., 2008. Characteristics of mineralization at the main zone of the Clarence Stream Gold Deposit, Southwestern New Brunswick, Canada: evidence for an intrusion-related gold system in the Northern Appalachian Orogen. Exploration and Mining Geology 17:13-49.

Tischendorf, G., Rieder, M., Forster, H.J., Gottesmann, B., Guidotti, C.V., 2004. A new graphical presentation and subdivision of potassium micas. Mineralogical Magazine 68, 649-667.

Tuduri, J., 2005. Processus de formation et relations spatio-temporelles des minéralisations à or et argent en contexte volcanique Précambrien (Jbel Saghro, Anti-Atlas, Maroc). Implications sur les relations déformation-magmatisme-volcanisme-hydrothermalisme. Université d'Orléans, Orléans, France, p. 428.

Tuduri, J., Chauvet, A., Ennaciri, A., Barbanson, L., 2006. Modèle de formation du gisement d'argent d'Imiter (Anti-Atlas oriental, Maroc). Nouveaux apports de l'analyse structurale et minéralogique. Comptes Rendus Geoscience 338, 253-261.

Tunks A.J., Cooke D.R., 2007 Geological and structural controls on gold mineralization in the Tanami District, Northern Territory. Mineralium Deposita 42:107-26.

Vallance, J., Cathelineau, M., Boiron, M.C., Fourcade, S., Shepherd, T.J., Naden, J., 2003. Fluid-rock interactions and the role of late Hercynian aplite intrusion in the genesis of the Castromil gold deposit, northern Portugal. Chemical Geology 194, 201-224.

Van Achterbergh, E., Ryan, C.G., Jackson, S.E., Griffin, W.L., 2001. Data reduction software for LA-ICPMS: appendix, in: Sylvester, P.J. (Ed.), Laser Ablation-ICP Mass Spectrometry in the Earth Sciences: Principles and Applications. Mineralogical Association of Canada (MAC) Short Courses Ottawa, Ontario, Canada, pp. 239-243.

Walsh, G.J., Benziane, F., Aleinikoff, J.N., Harrison, R.W., Yazidi, A., Burton, W.C., Quick, J.E., Saadane, A., 2012. Neoproterozoic tectonic evolution of the Jebel Saghro and Bou Azzer—El Graara inliers, eastern and central Anti-Atlas, Morocco. Precambrian Research 216–219, 23-62.

Whitney, D.L., Evans, B.W., 2010. Abbreviations for names of rock-forming minerals. American Mineralogist 95, 185-187.

Wilkinson, J.J., 1991. Volatile production during contact metamorphism: the role of organic matter in pelites. Journal of the Geological Society 148, 731-736.

Yardley B.W.D., 2005. 100th Anniversary Special Paper: metal concentrations in crustal fluids and their relationship to ore formation. Economic Geology 100:613-32.

Yardley B.W.D., Cleverley J.S., 2015. The role of metamorphic fluids in the formation of ore deposits. Geological Society, London, Special Publications 393:117-34.

Figure captions

Fig. 1. (a) Location of the Anti-Atlas belt at the northern limit of the West African Craton, modified after Milési et al., (2004). (b) Main geological units of the Moroccan Anti-Atlas, modified from Hollard et al. (1985); Thomas et al. (2004); Walsh et al. (2012) and Ikenne et al. (2017). Inliers - BD: Bas Drâa; If: Ifni; K: Kerdous; TA: Tagragra d'Akka; Im: Igherm; TT: Tagragra de Tata; Ig: Iguerda; AM: Agadir-Melloul; Z: Zenaga.

Fig. 2. Simplified geologic map of the Jbel Saghro, modified after Hindermeyer et al. (1977) and Walsh et al. (2012).

Fig. 3. (a) Geologic map of the Boumalne Neoproterozoic inlier modified after Benkirane (1987) and Tuduri (2005). (b) Structural map of the Thaghassa area.

Fig. 4. Stereographic projection (Schmidt's lower hemisphere equal-area projection) of (a): foliation planes, (b): stretching lineation, (c): quartzo-feldspathic, aplite, and pegmatite sills and tension gashes, and (d): intermediate and striped quartz veins and related tension gashes. Planes are represented by their respective poles.

Fig. 5. Macro and microstructures illustrating distribution of metamorphic record and kinematics of the ductile deformation in the Boumalne inlier. (a) Main chlorite zone feature consisting in top-to-the-south shearing showing synkinematic crystallization of chlorite within S-C bands, plane polarized light microscopy. (b) S_{0-1} foliation and related lineation marked by elongate metamorphic spots that affect the outer hornfels zone. Typical structures observed the outer hornfels zone showing: (c) syn to late kinematic metamorphic spot showing rolling structure consistent with a top-to-the south shearing sense, and (d) sets of S-C structures consistent with a top-to-the north shearing sense. Note the asymmetric tails composed of biotite and the late growth of white mica, plane polarized light microscopy. Typical features from the inner hornfels zone showing: (e) K-feldpar, quartz, and biotite assemblage overprinted by post-kinematic, poikilitic muscovite, and (f) leucosome of quartz and altered K-feldspar defining a leucocratic band biotite selvedge, plane polarized light microscopy. Abbreviations of Whitney and Evans, (2010).

Fig. 6. Macrostructures and microstructures illustrating the leucocratic, aplitic, and pegmatitic features. (a) Different generations of concordant and discordant leucocratic quartzo-feldspathic structures emplaced within the inner hornfels zone. "En-echelon" tension-gash geometry demonstrates that their formation was coeval with dextral shearing. (b) Normal shearing and boudinage affecting the leucocratic structures. (c) Biotite selvedges developed on both sides of a deformed K-feldspar, plagioclase, and quartz leucocratic discordant structure within the inner hornfels zone. Note feldspar alteration and the absence of muscovite, plane polarized light microscopy. (d) Typical texture of K-feldspar, plagioclase (both altered), and quartz leucocratic concordant sheets within the inner hornfels zone. Muscovite occurs as late crystals. Note discrete biotite selvedge on the side of the veinlets, cross polarized light microscopy. (e) Dextral pull-apart geometry filled by pegmatite dyke. (f) Boudinage of aplitic sill. (g) Typical texture of an aplitic sill exhibiting quartz, altered plagioclase, and K feldspar, garnet, and muscovite, plane polarized light microscopy. Abbreviations of Whitney and Evans (2010).

Fig. 7. Macrostructures and microstructures illustrating the intermediate veins and muscovite alteration halos. (a) General aspect of N120°E trending intermediate veins developed within more competent layers. Arrows show intermediate veins. (b) Intermediate veins developed within more competent layers occurring oblique to the foliation. (c) Foliation-parallel intermediate veins developing a thin feldspar-rich selvedge and a quartz-rich core, emplaced within the inner hornfels rocks. (d) Intermediate veins filled by quartz which is abundant, feldspar, muscovite, and tourmaline assemblage, cross polarized light microscopy. Note that the vein lies at a small angle with foliation because it tends to become sigmoidal at its end. (e) Foliation-parallel veins displaying selvedge of feldspar, apatite, quartz, and a quartz-only core. IHR: Inner Hornfels Rock. Dotted line corresponds to host rock contact, plane polarized light microscopy. (f) Typical alteration halo comprising mainly muscovite and quartz developed in aplite sills, cross polarized light microscopy. (g) Microphotography illustrating alteration of earlier large poikilitic

muscovites (Ms1) during muscovitization and showing corrosion of their crystal borders. Muscovites from the alteration halo (Ms2) are widely developed in the metagreywacke. Note that quartz vein post-dates the muscovite alteration stage, cross polarized light microscopy. Abbreviations of Whitney and Evans, (2010).

Fig. 8. Macrostructures illustrating the gold-bearing quartz vein stage. (a) Allure of the striped foliation vein parallel to the foliation. (b) Close-up view of the cross-cutting relationships between aplo-pegmatite sills and striped quartz veins. There, the aplo-pegmatite sill is clearly hosting the hydrothermal vein. Note the pull-apart geometry describing dextral strike-slip faulting. (c) Internal layering texture usually parallel to the foliation and thus defining the striped foliation vein structure. (d) Relationship between ~ E-W striped quartz veins and related N120-150°E tension gashes. Vein system is hosted by outer hornfelsed schists.

Fig. 9. Microtextural characteristics of striped quartz veins. (a) Internal texture of striped foliation vein. Elongate quartz grains are oblique with respect to vein walls and inclusions bands, cross polarized light microscopy. (b) Inclusions bands parallel to vein wall within striped foliation veins. Note that inclusion bands are parallel to the vein direction, wavy, and affected by stylolite plans, plane polarized light microscopy. (c) Inclusion bands characterized by foliation particles – altered muscovites (Ms1) from host-rock fragments - and neo-formed radial sericite, cross polarized light microscopy. (d-f) Recrystallization process associated with the ongoing and progressive deformation. Thin recrystallized fissures and clear zone are highlighted by arrows (d), and zones invaded by micro-grains showing dextral shear zone (e and f) affect the large quartz grains, cross polarized light microscopy. (g) General features of N040-050°E striped veins. Note the lower angle (<< 45°) between elongated grain and vein wall and the more elongated quartz grains, cross polarized light microscopy. (h) Zoned comb quartz grains describing geodic infilling within tension-gashes. White arrows show quartz <c> axis that are normal to the microphotography, cross polarized light microscopy. Abbreviations of Whitney and Evans, (2010).

Fig. 10. Chemical characteristics of muscovites. (a) Diagram illustrating the ideal dioctahedral substitutions of the Thaghassa muscovites after Guidotti (1984). (b) Application of the Monier and Robert (1986) thermometer on the magmatic - hydrothermal muscovites of the studied area.

Fig. 11. Backscattered secondary electron images of mineralized assemblages. (a) Arsenopyrite inclusion and massive pyrite presenting a zoning related to various As amounts. (b) Submicroscopic inclusions of galena within zoned pyrite 2. (c) Relations between the two generations of arsenopyrites. (d) Cassiterite and chalcopyrite inclusions within arsenopyrite. (e) Microscopic electrum grains associated with freibergite within pyrite 2. (f) Microcracks within zoned pyrite filled by chalcopyrite, arsenopyrite 2 and freibergite.

Fig. 12. Photomicrographs of quartz hosted Fluid Inclusion Assemblages. (a) Type A primary fluid inclusions with nearly single-phase vapour (V) phase from aplite sill. (b) Type B two phases (LV) primary fluid inclusions with variable volume percent vapour in an intermediate vein. Arrows show volume percent vapour higher than 90% and lower than 50%. (c) Type B two phases (LV) secondary fluid inclusions from an intermediate vein. (d) Type C two phase (Lv) primary fluid inclusions from striped foliation vein. (e) Type C two phase (Lv) secondary fluid inclusions from striped foliation vein. (f) Type D (Lv) secondary fluid inclusions observed in striped vein. GZL: Growth Zone Limit. PSI: Plane of Secondary Inclusions. All pictures are plane polarized light microscopy.

Fig. 13. (a) Homogenization temperature vs. ice melting of the fluid inclusion associations measured in the Thaghassa deposit. Note that because studied type A inclusions only provide either $Th_{(v)}$ *or* $Tm_{(ice)}$ *in different FIA, no data are presented in the graph. (b) Ternary diagram showing vapour bubble composition in term of* CO_2-CH_4-N_2 *from laser Raman analysis for fluid inclusions. Note that type C inclusions are* N_2 *free and that Type D inclusions are lacking because they are composed of* H_2O-*NaCl solely.*

Fig. 14. Simplified geological map of the Boumalne basin inlier showing the RSCM Tmax results and sample location.

Fig. 15. Tera & Wasserburg (inverse Concordia) diagram representing isotopic data of U and Pb for the Ikniwn granodiorite (SO64).

Fig. 16. Block diagram summarizing the geometry and the distribution of the different structural features and any type of veins observed in the Thaghassa deposit, north of the Ikniwn granodiorite.

Fig. 17. Interpretative schema illustrating the continuous and progressive model of vein formation since the aplo-pegmatite stage (a), intermediate veins (b), and striped foliation quartz veins (c). Note that all stages are controlled by an ESE-WNW shortening direction.

Fig. 18. Regional tectono-magmatic evolution of the Thaghassa area illustrating the link between structures, vein formation, and granite emplacement. (a) The first event is related to the earlier granodiorite emplacement and formation of the south-verging character. (b) Leucocratic segregation, aplite sill emplacement, and subsequent formation of striped foliation veins are coeval with a general dextral-normal shearing. (c) Late tectono-volcanic event and volcanic dyke injection. X, Y and Z are the three strain axes. Z is parallel to the shortening direction.

Supplementary data

SA1 - Chemical compositions (EPMA) and structural formulae (apfu) of muscovite, pyrite, arsenopyrite, sphalerite, loellingite, tetrahedrite, freibergite and electrum

SA2 - Operating conditions for the LA-ICP-MS equipment

SA3 - LA-ICP-MS data for zircons

Type	Muscovites from aplites				Muscovites from pegmatites				Poikilitic muscovites from "aureole"				Muscovites from intermediate veins				Muscovites from alteration halos				Muscovites from striped foliation veins			
n.	23				29				46				17				22				22			
	Av.	2σ	Min	Max	Av.	2σ	Min	Max	Av.	2σ	Min	Max	Av.	2σ	Min	Max	Av.	2σ	Min	Max	Av.	2σ	Min	Max
Chemical composition (oxides wt%)																								
FeO	0.93	0.41	0.22	1.48	1.07	0.25	0.77	1.80	0.79	0.21	0.14	1.41	0.95	0.14	0.63	1.20	1.15	0.16	0.79	1.55	1.45	0.29	1.03	2.04
Na_2O	0.40	0.09	0.18	0.55	0.51	0.14	0.24	0.76	0.39	0.14	0.18	0.70	0.40	0.04	0.37	0.52	0.19	0.05	0.12	0.31	0.12	0.03	0.05	0.16
K_2O	10.84	0.25	10.44	11.23	10.60	0.42	8.80	11.13	10.51	0.43	9.00	11.27	10.29	0.24	9.88	10.58	10.53	0.46	9.50	11.07	10.02	0.25	9.43	10.51
MnO	0.02	0.04	0.00	0.11	0.00	0.02	bdl	0.11	0.01	0.03	bdl	0.14	0.00	0.01	bdl	0.04	0.03	0.05	bdl	0.14	0.06	0.07	bdl	0.21
SiO_2	44.88	0.68	43.34	45.87	45.29	1.50	42.08	46.94	45.78	0.48	44.47	47.32	45.27	0.51	44.64	46.55	45.71	1.09	43.37	47.15	47.84	0.84	47.21	50.17
CaO	bdl	bdl	bdl	bdl	0.01	0.03	bdl	0.18	0.00	0.01	bdl	0.03	bdl	bdl	bdl	bdl	0.01	0.02	bdl	0.10	0.01	0.01	bdl	0.04
Cr_2O_3	0.00	0.02	bdl	0.09	0.00	0.01	bdl	0.05	0.01	0.03	bdl	0.10	0.02	0.05	bdl	0.13	0.02	0.04	bdl	0.14	bdl	bdl	bdl	bdl
Al_2O_3	36.37	0.88	33.83	37.81	35.57	0.72	33.24	36.66	35.79	0.76	34.50	37.12	35.47	0.24	35.06	35.93	32.88	0.59	32.06	34.28	31.35	0.62	30.25	32.39
TiO_2	0.04	0.09	bdl	0.32	0.13	0.09	bdl	0.31	0.64	0.28	0.10	1.33	0.44	0.15	0.23	0.75	0.29	0.50	bdl	1.95	0.24	0.09	0.08	0.46
MgO	0.39	0.26	bdl	0.96	0.37	0.14	0.10	0.81	0.57	0.10	0.40	0.79	0.74	0.09	0.57	0.93	1.15	0.33	0.56	1.76	2.32	0.25	1.99	3.04
V_2O_3	0.01	0.03	bdl	0.11	0.00	0.02	bdl	0.12	0.02	0.04	bdl	0.15	bdl	bdl	bdl	bdl	0.01	0.03	bdl	0.09	bdl	bdl	bdl	bdl
F	0.12	0.17	bdl	0.57	0.15	0.20	bdl	0.63	0.13	0.20	bdl	0.74	0.25	0.19	bdl	0.58	0.07	0.07	bdl	0.19	0.33	0.22	bdl	0.68
Cl	0.00	0.00	bdl	0.01	0.00	0.01	bdl	0.03	0.01	0.01	bdl	0.03	0.00	0.00	bdl	0.02	0.01	0.02	bdl	0.06	0.01	0.02	bdl	0.05
Li_2O	0.03	0.05	0.00	0.19	0.04	0.06	0.00	0.21	0.04	0.06	0.00	0.26	0.07	0.06	0.00	0.19	0.01	0.01	0.00	0.04	0.00	0.07	0.00	0.04
Σ	94.04				93.75				94.68				93.95				92.07				94.48			
Structural formulas (apfu) based on 11 oxygens																								
Si (T)	3.03	0.03	2.99	3.08	3.07	0.04	2.98	3.15	3.07	0.02	3.03	3.11	3.06	0.02	3.03	3.09	3.15	0.05	3.03	3.22	3.26	0.03	3.19	3.31
Al (T)	0.97	0.03	0.92	1.01	0.93	0.04	0.85	1.02	0.93	0.02	0.89	0.97	0.94	0.02	0.91	0.97	0.85	0.05	0.78	0.97	0.74	0.03	0.69	0.81
□ vac.	0.96	0.02	0.91	1.00	0.97	0.03	0.89	1.01	0.97	0.02	0.90	1.01	0.94	0.02	0.90	0.97	0.97	0.02	0.93	0.99	0.90	0.03	0.84	0.96
Ti (M)	0.00	0.00	bdl	0.02	0.01	0.00	bdl	0.02	0.03	0.01	0.00	0.07	0.02	0.01	0.01	0.04	0.02	0.03	bdl	0.10	0.01	0.00	bdl	0.02
Cr (M)	0.00	0.00	bdl	0.01	0.00	0.00	bdl	0.00	0.00	0.00	bdl	0.01	0.00	0.00	bdl	0.01	0.00	0.00	bdl	0.01	bdl	bdl	bdl	bdl
V (M)	0.00	0.00	bdl	0.01	0.00	0.00	bdl	0.01	0.00	0.00	bdl	0.01	bdl	bdl	bdl	bdl	0.00	0.00	bdl	0.01	bdl	bdl	bdl	bdl
Al (M)	1.93	0.04	1.83	2.03	1.91	0.03	1.86	1.95	1.89	0.03	1.83	1.95	1.89	0.01	1.86	1.91	1.82	0.03	1.76	1.88	1.74	0.02	1.68	1.79
Fe (M)	0.05	0.02	0.01	0.09	0.06	0.01	0.04	0.10	0.04	0.01	0.01	0.08	0.05	0.01	0.04	0.07	0.07	0.01	0.05	0.09	0.08	0.02	0.06	0.12
Mg	0.00	0.00	bdl	0.01	0.00	0.00	0.00	0.00	0.00	0.00	0.00	0.00	0.00	0.00	0.00	0.00	0.01	0.00	0.00	0.01	0.02	0.00	0.02	0.03

(M)	4	3		0	4	01	1	9	6	01	4	8	7	01	6	9	2	03	6	8	3	02	0	1
Mn (M)	0.00	0.00	0.00	0.01	0.00	0.00	bdl	0.01	0.00	0.00	bdl	0.01	0.00	0.00	bdl	0.00	0.00	0.00	bdl	0.01	0.00	0.00	bdl	0.01
Li (M)	0.01	0.01	0.00	0.05	0.01	0.02	0.00	0.06	0.01	0.02	0.00	0.07	0.02	0.02	0.00	0.05	0.00	0.00	0.00	0.01	0.03	0.02	0.00	0.06
Ca (I)	bdl	bdl	bdl	bdl	0.00	0.00	bdl	0.01	0.00	0.00	bdl	0.00	bdl	bdl	bdl	bdl	0.00	0.00	bdl	0.01	bdl	bdl	bdl	bdl
Na (I)	0.05	0.01	0.02	0.07	0.07	0.02	0.03	0.10	0.05	0.02	0.02	0.09	0.06	0.01	0.05	0.07	0.03	0.01	0.02	0.04	0.02	0.00	0.01	0.02
K (I)	0.94	0.03	0.89	0.99	0.92	0.04	0.75	0.97	0.90	0.04	0.77	0.97	0.89	0.02	0.86	0.91	0.93	0.04	0.83	0.98	0.86	0.02	0.81	0.90
F	0.03	0.04	bdl	0.12	0.03	0.04	bdl	0.14	0.03	0.04	bdl	0.16	0.05	0.04	bdl	0.12	0.02	0.01	bdl	0.04	0.07	0.05	bdl	0.14
Cl	0.00	0.00	bdl	0.00	0.00	0.00	bdl	0.00	0.00	0.00	bdl	0.00	0.00	0.00	bdl	0.00	0.00	0.00	bdl	0.01	0.00	0.00	bdl	0.01
OH	1.97	0.04	1.88	2.00	1.97	0.04	1.86	2.00	1.97	0.04	1.84	2.00	1.95	0.04	1.88	2.00	1.98	0.01	1.96	2.00	1.93	0.05	1.86	2.00
mgli	0.03	0.03	-0.04	0.10	0.02	0.02	-0.02	0.06	0.05	0.02	-0.02	0.08	0.06	0.02	0.03	0.08	0.11	0.03	0.06	0.17	0.21	0.03	0.17	0.31
feal	-1.88	0.07	-1.98	-1.73	-1.85	0.04	-1.90	-1.74	-1.81	0.05	-1.94	-1.71	-1.82	0.02	-1.86	-1.77	-1.74	0.05	-1.79	-1.59	-1.65	0.04	-1.72	-1.56
R^{3+}_{total}	2.90	0.06	2.75	2.99	2.84	0.06	2.72	2.96	2.83	0.04	2.75	2.90	2.83	0.02	2.78	2.87	2.67	0.06	2.61	2.83	2.48	0.04	2.41	2.57
R*	0.13	0.07	0.02	0.26	0.18	0.06	0.09	0.31	0.20	0.03	0.14	0.24	0.21	0.02	0.18	0.27	0.35	0.06	0.20	0.45	0.59	0.05	0.52	0.67
% ph	18.75	10.18	3.21	39.54	20.76	5.18	13.27	35.37	26.46	4.40	15.46	35.11	29.59	3.05	24.12	35.52	39.72	5.60	32.51	51.16	63.63	6.73	51.23	81.54

Notes: bdl is below the detection limit; mgli = Mg-Li and feal = Fe+Mn+Ti-$^{[6]}$Al) with respect to Tischendorf et al. (2004) recommendations; R^{3+}_{total} = Al + V + Cr; R* = Fe+Mg+Ti+(Si-3); % ph = phengitic component as percentage of the ration (Fe+Mg+Ti+Mn)/(Fe+Mg+Ti+Mn+$^{[6]}$Al) assumed that phengite end member ratio = 0.25 (100 %) and muscovite end member ratio = 0 (0 %).

Type	Core of pyrite				Pyrite external part								Arsenopyrite type 1				Arsenopyrite type 2			
n.	111				n = 49 of As-rich bands				n = 22 of As-poor band				16				44			
	Av.	2σ	Min	Max	Av.	2σ	Min	Max	Av.	2σ	Min	Max	Av.	2σ	Min	Max	Av.	2σ	Min	Max
Chemical composition (elements wt%)																				
Cu	0.02	0.17	bdl	1.79	0.00	0.01	bdl	0.06	bdl	bdl	bdl	bdl	bdl	bdl	bdl	bdl	bdl	bdl	bdl	bdl
S	52.63	0.37	51.73	53.48	51.79	0.32	51.216	52.57	53.24	0.27	52.82	53.70	19.18	0.78	18.31	21.11	18.29	0.39	17.45	19.27
Fe	46.12	0.27	45.20	46.59	45.73	0.32	44.547	46.25	46.25	0.31	45.69	46.90	33.50	0.53	32.62	34.36	33.02	0.49	31.97	34.20
Sb	bdl	bdl	bdl	bdl	bdl	bdl	bdl	bdl	bdl	bdl	bdl	bdl	0.49	0.29	0.15	1.20	0.46	0.27	0.133	1.20
As	0.71	0.29	0.20	1.19	2.01	0.47	1.21	2.64	0.08	0.06	bdl	0.16	46.24	1.01	43.61	46.951	47.58	0.39	47.07	48.55
Zn	bdl	0.00	bdl	0.03	bdl	bdl	bdl	bdl	bdl	bdl	bdl	bdl	bdl	bdl	bdl	bdl	bdl	bdl	bdl	bdl
Pb	0.09	0.19	bdl	1.40	0.07	0.09	bdl	0.26	0.07	0.10	bdl	0.29	0.03	0.07	bdl	0.17	0.05	0.07	bdl	0.16
Mn	bdl	bdl	bdl	bdl	0.03	0.04	bdl	0.06	bdl	bdl	bdl	bdl	bdl	bdl	bdl	bdl	bdl	bdl	bdl	bdl
Ag	bdl	bdl	bdl	bdl	0.00	0.01	bdl	0.05	0.01	0.01	bdl	0.05	bdl	bdl	bdl	bdl	bdl	bdl	bdl	bdl
Se	bdl	bdl	bdl	bdl	bdl	bdl	bdl	bdl	bdl	bdl	bdl	bdl	0.01	0.02	bdl	0.05	0.02	0.04	bdl	0.09
Te	0.00	0.00	bdl	0.03	bdl	bdl	bdl	bdl	bdl	bdl	bdl	bdl	bdl	bdl	bdl	bdl	bdl	bdl	bdl	bdl
Au	bdl	bdl	bdl	bdl	bdl	bdl	bdl	bdl	bdl	bdl	bdl	bdl	bdl	bdl	bdl	bdl	bdl	bdl	bdl	bdl
Cd	bdl	bdl	bdl	bdl	bdl	bdl	bdl	bdl	bdl	bdl	bdl	bdl	bdl	bdl	bdl	bdl	bdl	bdl	bdl	bdl
Hg	bdl	bdl	bdl	bdl	bdl	bdl	bdl	bdl	bdl	bdl	bdl	bdl	bdl	bdl	bdl	bdl	bdl	bdl	bdl	bdl
Bi	0.04	0.06	bdl	0.20	0.04	0.07	bdl	0.24	0.03	0.06	bdl	0.18	bdl	bdl	bdl	bdl	bdl	bdl	bdl	bdl
Ni	0.03	0.06	bdl	0.38	0.10	0.15	bdl	0.61	0.03	0.05	bdl	0.17	0.04	0.11	bdl	0.43	0.23	0.26	bdl	1.06
Co	0.00	0.01	bdl	0.04	bdl	0.00	bdl	0.02	0.00	0.01	bdl	0.02	0.10	0.11	bdl	0.28	0.28	0.21	bdl	0.75
In	bdl	bdl	bdl	bdl	bdl	bdl	bdl	bdl	bdl	bdl	bdl	bdl	bdl	bdl	bdl	bdl	bdl	bdl	bdl	bdl
W	bdl	bdl	bdl	bdl	bdl	bdl	bdl	bdl	bdl	bdl	bdl	bdl	bdl	bdl	bdl	bdl	bdl	bdl	bdl	bdl
Mo	bdl	bdl	bdl	bdl	bdl	bdl	bdl	bdl	bdl	bdl	bdl	bdl	bdl	bdl	bdl	bdl	bdl	bdl	bdl	bdl
Total	99.64				99.77				99.71				99.59				99.93			
Normalized on 3 atoms																				
Cu	bdl	0.00	bdl	0.03	bdl	bdl	bdl	0.001	bdl	bdl	bdl	bdl	bdl	bdl	bdl	bdl	bdl	bdl	bdl	bdl
S	1.99	0.01	1.965	2.01	1.97	0.01	1.95	1.99	2.00	0.01	1.99	2.01	0.97	0.03	0.96	1.06	0.95	0.02	0.91	0.98
Fe	1.00	0.01	0.986	1.01	1.00	0.01	0.98	1.00	1.00	0.01	0.99	1.01	0.97	0.01	0.97	1.01	0.98	0.01	0.96	1.00
Sb	bdl	bdl	bdl	bdl	bdl	bdl	bdl	bdl	bdl	bdl	bdl	bdl	0.01	0.00	0.00	0.02	0.01	0.00	0.00	0.02
As	0.01	0.01	0.003	0.02	0.03	0.01	0.02	0.04	0.00	0.00	bdl	0.00	1.02	0.03	0.94	1.04	1.05	0.01	1.03	1.07
Zn	bdl	bdl	bdl	0.00	bdl	bdl	bdl	bdl	bdl	bdl	bdl	bdl	bdl	bdl	bdl	bdl	bdl	bdl	bdl	bdl
Pb	bdl	0.00	bdl	0.01	bdl	0.00	bdl	0.00	bdl	0.00	bdl	0.00	bdl	bdl	bdl	0.00	bdl	bdl	bdl	0.00
Mn	bdl	bdl	bdl	bdl	bdl	bdl	bdl	0.00	bdl	bdl	bdl	bdl	bdl	bdl	bdl	bdl	bdl	bdl	bdl	bdl
Ag	bdl	bdl	bdl	bdl	bdl	bdl	bdl	0.00	bdl	bdl	bdl	0.00	bdl	bdl	bdl	bdl	bdl	bdl	bdl	bdl
Se	bdl	bdl	bdl	bdl	bdl	bdl	bdl	bdl	bdl	bdl	bdl	bdl	bdl	bdl	bdl	0.00	bdl	bdl	bdl	0.00
Te	bdl	bdl	bdl	bdl	bdl	bdl	bdl	bdl	bdl	bdl	bdl	bdl	bdl	bdl	bdl	bdl	bdl	bdl	bdl	bdl
Au	bdl	bdl	bdl	bdl	bdl	bdl	bdl	bdl	bdl	bdl	bdl	bdl	bdl	bdl	bdl	bdl	bdl	bdl	bdl	bdl
Cd	bdl	bdl	bdl	bdl	bdl	bdl	bdl	bdl	bdl	bdl	bdl	bdl	bdl	bdl	bdl	bdl	bdl	bdl	bdl	bdl
Hg	bdl	bdl	bdl	bdl	bdl	bdl	bdl	bdl	bdl	bdl	bdl	bdl	bdl	bdl	bdl	bdl	bdl	bdl	bdl	bdl
Bi	bdl	bdl	bdl	0.00	bdl	bdl	bdl	0.00	bdl	bdl	bdl	0.00	bdl	bdl	bdl	bdl	bdl	bdl	bdl	bdl
Ni	0.00	0.00	bdl	0.01	0.00	0.00	bdl	0.01	0.00	0.00	bdl	0.00	0.00	0.00	bdl	0.01	0.01	0.01	bdl	0.03
Co	bdl	bdl	bdl	0.00	bdl	bdl	bdl	bdl	bdl	bdl	bdl	bdl	0.00	0.00	bdl	0.01	0.01	0.01	bdl	0.02
In	bdl	bdl	bdl	bdl	bdl	bdl	bdl	bdl	bdl	bdl	bdl	bdl	bdl	bdl	bdl	bdl	bdl	bdl	bdl	bdl
W	bdl	bdl	bdl	bdl	bdl	bdl	bdl	bdl	bdl	bdl	bdl	bdl	bdl	bdl	bdl	bdl	bdl	bdl	bdl	bdl
Mo	bdl	bdl	bdl	bdl	bdl	bdl	bdl	bdl	bdl	bdl	bdl	bdl	bdl	bdl	bdl	bdl	bdl	bdl	bdl	bdl

Notes: bdl is below the detection limit

Typ n.	Sphalerite 18				Loellingite 6				Tetrahedrite 6				Freibergite 15				Electrum 5			
	Av.	2σ	Min	Max	Av.	2σ	Min	Max	Av.	2σ	Min	Max	Av.	2σ	Min	Max	Av.	2σ	Min	Max
Chemical composition (elements wt%)																				
Cu	0.25	0.4	bdl	1.78	bdl	bdl	bdl	bdl	27.9	0.41	27.5	28.3	21.13	0.7	19.4	21.9	0.16	0.1	0.07	0.34
S	32.8	0.2	32.4	33.4	1.58	0.7	0.78	3.22	23.4	0.12	23.3	23.6	22.71	0.8	21.4	24.4	0.75	0.5	0.28	1.32
Fe	7.78	0.6	6.52	8.95	26.85	0.9	25.2	27.8	6.01	0.12	5.80	6.22	6.35	1.7	3.98	9.49	1.934	0.2	1.78	2.28
Sb	bdl	bdl	bdl	bdl	0.35	0.1	0.17	0.57	27.3	0.87	26.4	28.2	26.19	1.0	24.2	27.4	0.87	0.1	0.73	0.96
As	0.02	0.0	bdl	0.11	70.64	0.9	69.2	71.8	0.65	0.05	0.57	0.72	0.66	0.2	0.43	1.58	bdl	bdl	bdl	bdl
Zn	56.6	0.9	54.3	58.2	bdl	bdl	bdl	bdl	1.15	0.04	1.10	1.22	1.49	0.7	0.69	2.87	bdl	bdl	bdl	bdl
Pb	0.03	0.0	bdl	0.13	bdl	bdl	bdl	bdl	bdl	bdl	bdl	bdl	0.32	1.1	bdl	4.26	0.03	0.0	bdl	0.12
Mn	0.50	0.0	0.38	0.63	bdl	bdl	bdl	bdl	bdl	bdl	bdl	bdl	bdl	bdl	bdl	bdl	bdl	bdl	bdl	bdl
Ag	bdl	bdl	bdl	bdl	bdl	bdl	bdl	bdl	12.1	0.16	11.9	12.3	21.46	1.6	18.7	24.8	46.52	0.7	45.8	47.4
Se	bdl	bdl	bdl	bdl	bdl	bdl	bdl	bdl	bdl	bdl	bdl	bdl	bdl	bdl	bdl	bdl	bdl	bdl	bdl	bdl
Te	bdl	bdl	bdl	bdl	bdl	bdl	bdl	bdl	bdl	bdl	bdl	bdl	bdl	bdl	bdl	bdl	bdl	bdl	bdl	bdl
Au	bdl	bdl	bdl	bdl	bdl	bdl	bdl	bdl	bdl	bdl	bdl	bdl	bdl	bdl	bdl	bdl	50.30	0.4	49.8	50.8
Cd	0.29	0.0	0.14	0.47	bdl	bdl	bdl	bdl	bdl	bdl	bdl	bdl	0.10	0.0	bdl	0.20	0.34	0.0	0.26	0.41
Hg	0.01	0.0	bdl	0.22	bdl	bdl	bdl	bdl	bdl	bdl	bdl	bdl	bdl	bdl	bdl	bdl	1.17	0.0	1.05	1.23
Bi	0.01	0.0	bdl	0.13	bdl	bdl	bdl	bdl	bdl	bdl	bdl	bdl	bdl	bdl	bdl	bdl	bdl	bdl	bdl	bdl
Ni	bdl	bdl	bdl	bdl	1.37	0.4	0.94	1.86	bdl	bdl	bdl	bdl	bdl	bdl	bdl	bdl	bdl	bdl	bdl	bdl
Co	bdl	bdl	bdl	bdl	0.35	0.0	0.32	0.41	bdl	bdl	bdl	bdl	bdl	bdl	bdl	bdl	bdl	bdl	bdl	bdl
In	bdl	bdl	bdl	bdl	bdl	bdl	bdl	bdl	bdl	bdl	bdl	bdl	bdl	bdl	bdl	bdl	bdl	bdl	bdl	bdl
W	bdl	bdl	bdl	bdl	bdl	bdl	bdl	bdl	bdl	bdl	bdl	bdl	bdl	bdl	bdl	bdl	bdl	bdl	bdl	bdl
Mo	bdl	bdl	bdl	bdl	bdl	bdl	bdl	bdl	bdl	bdl	bdl	bdl	bdl	bdl	bdl	bdl	bdl	bdl	bdl	bdl
Total	98.4				101.1				98.6				100.4				102.0			
	Normalized on 2				Normalized on 3 atoms				Normalized on 29 atoms				Normalized on 29				Normalized on 1 atoms			
Cu	0.00	0.0	bdl	0.03	bdl	bdl	bdl	bdl	7.75	0.04	7.71	7.82	6.02	0.2	5.61	6.38	0.00	0.0	0.00	0.00
S	1.00	0.0	0.99	1.01	0.10	0.0	0.05	0.20	12.9	0.10	12.8	13.0	12.82	0.2	12.5	13.2	0.03	0.0	0.01	0.05
Fe	0.14	0.0	0.11	0.16	0.97	0.0	0.92	1.00	1.90	0.03	1.85	1.94	2.05	0.5	1.35	2.97	0.05	0.0	0.04	0.05
Sb	bdl	bdl	bdl	bdl	0.01	0.0	0.00	0.01	3.97	0.09	3.85	4.06	3.90	0.2	3.48	4.11	0.01	0.0	0.00	0.01
As	bdl	0.0	bdl	0.00	1.90	0.0	1.81	1.96	0.15	0.01	0.13	0.17	0.16	0.0	0.11	0.37	bdl	bdl	bdl	bdl
Zn	0.85	0.0	0.81	0.87	bdl	bdl	bdl	bdl	0.31	0.01	0.30	0.33	0.41	0.2	0.20	0.84	bdl	bdl	bdl	bdl
Pb	bdl	bdl	bdl	0.00	bdl	bdl	bdl	bdl	bdl	bdl	bdl	bdl	0.03	0.1	bdl	0.39	bdl	bdl	bdl	0.00
Mn	0.01	0.0	0.01	0.01	bdl	bdl	bdl	bdl	bdl	bdl	bdl	bdl	bdl	bdl	bdl	bdl	bdl	bdl	bdl	bdl
Ag	bdl	bdl	bdl	bdl	bdl	bdl	bdl	bdl	1.98	0.04	1.93	2.04	3.61	0.3	3.03	4.27	0.57	0.0	0.55	0.58
Se	bdl	bdl	bdl	bdl	bdl	bdl	bdl	bdl	bdl	bdl	bdl	bdl	bdl	bdl	bdl	bdl	bdl	bdl	bdl	bdl
Te	bdl	bdl	bdl	bdl	bdl	bdl	bdl	bdl	bdl	bdl	bdl	bdl	bdl	bdl	bdl	bdl	bdl	bdl	bdl	bdl
Au	bdl	bdl	bdl	bdl	bdl	bdl	bdl	bdl	bdl	bdl	bdl	bdl	bdl	bdl	bdl	bdl	0.34	0.0	0.32	0.35
Cd	0.0	0.0	0.00	0.00	bdl	bdl	bdl	bdl	bdl	bdl	bdl	bdl	0.02	0.0	bdl	0.03	0.00	0.0	0.00	0.01
Hg	bdl	bdl	bdl	0.00	bdl	bdl	bdl	bdl	bdl	bdl	bdl	bdl	bdl	bdl	bdl	bdl	0.01	0.0	0.01	0.01
Bi	bdl	bdl	bdl	bdl	bdl	bdl	bdl	bdl	bdl	bdl	bdl	bdl	bdl	bdl	bdl	bdl	bdl	bdl	bdl	bdl
Ni	bdl	bdl	bdl	0.00	0.02	0.0	bdl	0.07	bdl	bdl	bdl	bdl	bdl	bdl	bdl	bdl	bdl	bdl	bdl	bdl
Co	bdl	bdl	bdl	bdl	0.01	0.0	bdl	0.01	bdl	bdl	bdl	bdl	bdl	bdl	bdl	bdl	bdl	bdl	bdl	bdl
In	bdl	bdl	bdl	bdl	bdl	bdl	bdl	bdl	bdl	bdl	bdl	bdl	bdl	bdl	bdl	bdl	bdl	bdl	bdl	bdl
W	bdl	bdl	bdl	bdl	bdl	bdl	bdl	bdl	bdl	bdl	bdl	bdl	bdl	bdl	bdl	bdl	bdl	bdl	bdl	bdl
Mo	bdl	bdl	bdl	bdl	bdl	bdl	bdl	bdl	bdl	bdl	bdl	bdl	bdl	bdl	bdl	bdl	bdl	bdl	bdl	bdl

Notes: bdl is below the detection limit

Appendix 2: Operating conditions for the LA-ICP-MS equipment

Laboratory & Sample Preparation	
Laboratory name	Géosciences Rennes, UMR CNRS 6118, Rennes, France
Sample type/mineral	zircon
Sample preparation	Thin-section – SO64
Imaging	Using a SEM at BRGM (Orléans, France).
Laser ablation system	
Make, Model & type	ESI NWR193UC, Excimer
Ablation cell	ESI NWR TwoVol2
Laser wavelength	193 nm
Pulse width	< 5 ns
Fluence	6.6 J/cm-2
Repetition rate	4 Hz
Spot size	25 µm
Sampling mode / pattern	Single spot
Carrier gas	100% He, Ar make-up gas and N2 (3 ml/mn) combined using in-house smoothing device
Background collection	20 seconds
Ablation duration	60 seconds
Wash-out delay	15 seconds
Cell carrier gas flow (He)	0.75 l/min
ICP-MS Instrument	
Make, Model & type	Agilent 7700x, Q-ICP-MS
Sample introduction	Via conventional tubing
RF power	1350W
Sampler, skimmer cones	Ni
Extraction lenses	X type
Make-up gas flow (Ar)	0.85 l/min
Detection system	Single collector secondary electron multiplier
Data acquisition protocol	Time-resolved analysis
Scanning mode	Peak hopping, one point per peak
Detector mode	Pulse counting, dead time correction applied, and analog mode when signal intensity > ~ 10^6 cps
Masses measured	^{204}(Hg + Pb), ^{206}Pb, ^{207}Pb, ^{208}Pb, ^{232}Th, ^{238}U
Integration time per peak	10-30 ms
Sensitivity / Efficiency	20000 cps/ppm Pb (50µm, 10Hz)
Data Processing	
Gas blank	20 seconds on-peak
Calibration strategy	GJ1 zircon standard used as primary reference material, Plešovice used as secondary reference material (quality control)
Reference Material info	GJ1 (Jackson et al., 2004) Plešovice (Slama et al., 2008)
Data processing package used	GLITTER ® (van Achterbergh et al., 2001)
Quality control / Validation	Plešovice: concordia age = 337.1 ± 1.2 Ma (N=46; MSWD=0.5)

Analysis #	Pb (ppm)	U (ppm)	Th (ppm)	Th/U	Isotopic Ratios U238/Pb206	err %	Pb207/Pb206	err %	Conc.	Ages (Ma) Pb206/U238	Abs Err	Pb207/U235	Abs err
5	27	285	85	0.30	**10.668**	**1.2**	**0.0589**	**1.1**	10 0.5	578	6	575	6
6	22	244	64	0.26	**10.948**	**1.2**	**0.0603**	**1.1**	98. 2	563	6	574	6
7	22	246	67	0.27	**11.186**	**1.2**	**0.0600**	**1.1**	98. 2	552	6	562	5
8	27	290	111	0.38	**11.148**	**1.2**	**0.0590**	**1.1**	99. 6	554	6	556	5
9	22	247	61	0.25	11.252	1.2	0.0612	1.1	96. 7	549	6	568	6
10	22	239	57	0.24	**10.875**	**1.2**	**0.0591**	**1.2**	99. 8	567	6	568	6
11	35	388	87	0.22	**10.867**	**1.2**	**0.0591**	**1.1**	99. 8	568	6	568	5
14	59	640	295	0.46	11.252	1.2	0.0601	1.1	97. 9	549	6	561	5
18	26	281	109	0.39	10.892	1.2	0.0606	1.2	97. 9	566	6	578	6
19	12	129	37	0.29	11.141	1.2	0.0610	1.3	97. 0	554	6	571	6
20	~~9~~	102	28	0.28	**11.007**	**1.2**	**0.0606**	**1.3**	97. 8	561	6	573	6
21	11	118	36	0.31	**10.972**	**1.2**	**0.0601**	**1.3**	98. 5	562	6	571	6
22	14	163	43	0.26	11.371	1.2	0.0598	1.2	98. 2	543	6	553	6
23	21	247	71	0.29	11.498	1.2	0.0610	1.2	96. 4	538	6	558	6
24	14	154	44	0.29	11.226	1.2	0.0605	1.3	97. 6	550	6	564	6
25	16	175	47	0.27	**10.818**	**1.2**	**0.0601**	**1.2**	98. 6	570	6	578	6

Analyses in bold were used for concordia age calculation (red ellipses on figure 15)

Conc = (206Pb/238U age) x 100 / (207Pb/235U age)

Highlights

• First evidence of a Neoproterozoic intrusion-related gold deposit in North-West Africa

• Evidence for a progressive and continuous, structurally controlled, vein system formation

• Evolving fluid compositions highlighting the magmatic-hydrothermal transition

• Migmatized hornfels providing both magmatic and metamorphic fluids